



HAL
open science

Effect of pressure on the deformation of quartz aggregates in the presence of H₂O

Lucille Nègre, Holger Stünitz, Hugues Raimbourg, A. Lee, Jacques Précigout, P. Pongrac, P. Jeřábek

► **To cite this version:**

Lucille Nègre, Holger Stünitz, Hugues Raimbourg, A. Lee, Jacques Précigout, et al.. Effect of pressure on the deformation of quartz aggregates in the presence of H₂O. *Journal of Structural Geology*, 2021, 148, pp.104351. <10.1016/j.jsg.2021.104351>. <insu-03201529>

HAL Id: insu-03201529

<https://insu.hal.science/insu-03201529v1>

Submitted on 19 Apr 2021

HAL is a multi-disciplinary open access archive for the deposit and dissemination of scientific research documents, whether they are published or not. The documents may come from teaching and research institutions in France or abroad, or from public or private research centers.

L'archive ouverte pluridisciplinaire **HAL**, est destinée au dépôt et à la diffusion de documents scientifiques de niveau recherche, publiés ou non, émanant des établissements d'enseignement et de recherche français ou étrangers, des laboratoires publics ou privés.

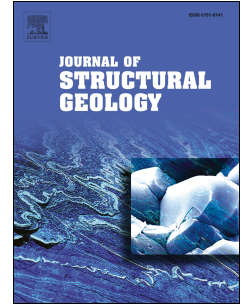


HAL Authorization

Journal Pre-proof

Effect of pressure on the deformation of quartz aggregates in the presence of H₂O

L. Nègre, H. Stünitz, H. Raimbourg, A. Lee, J. Précigout, P. Pongrac, P. Jeřábek



PII: S0191-8141(21)00075-4

DOI: <https://doi.org/10.1016/j.jsg.2021.104351>

Reference: SG 104351

To appear in: *Journal of Structural Geology*

Received Date: 8 December 2020

Revised Date: 9 April 2021

Accepted Date: 13 April 2021

Please cite this article as: Nègre, L., Stünitz, H., Raimbourg, H., Lee, A., Précigout, J., Pongrac, P., Jeřábek, P., Effect of pressure on the deformation of quartz aggregates in the presence of H₂O, *Journal of Structural Geology*, <https://doi.org/10.1016/j.jsg.2021.104351>.

This is a PDF file of an article that has undergone enhancements after acceptance, such as the addition of a cover page and metadata, and formatting for readability, but it is not yet the definitive version of record. This version will undergo additional copyediting, typesetting and review before it is published in its final form, but we are providing this version to give early visibility of the article. Please note that, during the production process, errors may be discovered which could affect the content, and all legal disclaimers that apply to the journal pertain.

© 2021 Published by Elsevier Ltd.

Author statement

All authors have read the manuscript and agree with its content.

Journal Pre-proof

1 **Effect of pressure on the deformation of quartz aggregates in** 2 **the presence of H₂O**

3 Authors: L. Nègre ^{a,*}, H. Stünitz ^{a,b}, H. Raimbourg ^a, A. Lee ^b, J. Précigout ^a, P.
4 Pongrac ^c, P. Jeřábek ^c

5 ^a Institut des Sciences de la Terre d'Orléans (ISTO), UMR 7327, CNRS/BRGM, Université
6 d'Orléans, 45071 Orléans, France

7 ^b Department of Geology, University of Tromsø, Dramsveien 201, 9037 Tromsø, Norway

8 ^c Institute of Petrology and Structural Geology, Faculty of Science, Charles University in Prague,
9 Albertov 6, 128 43 Prague, Czech Republic

10

11 Email addresses: lucille.negre@univ-orleans.fr (L. Nègre), holger.stunitz@uit.no (H.
12 Stünitz), hugues.raimbourg@univ-orleans.fr (H. Raimbourg), amicia.lee@uit.no (A.
13 Lee), jacques.precigout@univ-orleans.fr (J. Précigout), petar.pongrac@natur.cuni.cz
14 (P. Pongrac), jerabek.petr@natur.cuni.cz (P. Jeřábek)

15

16 Corresponding author: Institut des Sciences de la Terre d'Orléans (ISTO), 1a rue
17 de la Férollerie, 45100 Orléans, France, +332 38 25 50 27

18

19 Keywords: quartz deformation, quartz rheology, H₂O weakening, dynamic
20 recrystallization

22 Quartzite samples of high purity with a grain size of $\sim 200 \mu\text{m}$ have been
23 experimentally deformed by coaxial shortening in a solid medium apparatus at 900°C
24 and at confining pressures ranging from 0.6 to 2 GPa. Most samples have been
25 shortened by $\sim 30\%$ with 0.1 wt.% added H_2O . The samples deformed dominantly by
26 crystal plasticity (dislocation creep), and there is a systematic decrease of flow stress
27 with increasing confining pressure. Strain rate stepping tests yield stress exponents
28 of $n \sim 1.4$. The strain determined from individual grain shapes matches that
29 determined from bulk shortening. In addition to plastic strain, mode I cracks
30 developed in all samples, principally in the grain boundary regions. Recrystallized
31 material, visible through cathodoluminescence colours, forms by two mechanisms:
32 (1) progressive subgrain rotation and (2) cracking, nucleating small new grains. After
33 high-angle boundaries have been established, grain boundary migration takes place,
34 and a distinction of new grains nucleation origin (subgrain rotation or cracking) is
35 impossible. At higher pressure, there is more recrystallized material forming in the
36 deformed samples, and it is inferred that the inverse pressure dependence of flow
37 stress is caused by enhanced grain boundary migration at higher pressure,
38 consistent with previous studies.

40 Despite a long history of research since the early discovery of the effect of H₂O on
41 quartz rheology by Griggs and Blacic (1965), many aspects of H₂O weakening in
42 quartz are yet unresolved. One of these aspects is the clearly observed dependence
43 of the H₂O weakening on pressure: it had been suggested by Paterson and
44 Kekulawala, (1979), Tullis et al. (1979), Blacic (1981) and Mainprice and Paterson
45 (1984) that the confining pressure has an enhancing effect on the H₂O weakening
46 effect in quartz, speculating that pressure may positively affect the diffusive uptake of
47 H₂O. The seminal work by Kronenberg and Tullis (1984) clearly demonstrated and
48 quantified the increasing weakening of quartzite with increasing confining pressure in
49 the presence of H₂O. However, not much later it has been shown by Kronenberg et
50 al. (1986) and Gerretsen et al. (1989) that the diffusion of H₂O into quartz occurs at
51 rates far too slow (or not at all) to play a role in deformation experiments, and that
52 the infiltration of H₂O into quartz is achieved by microcracking in experiments. Thus,
53 the effect of pressure on deformation of quartz in the presence of H₂O had been
54 demonstrated but its cause was not very clear. Tullis and Yund (1989) have
55 presented a study of annealing deformed quartz crystals at different pressures in the
56 presence of H₂O and have shown that recovery and recrystallization are enhanced
57 by higher pressures.

58 In more recent studies of fine grained quartz material Rutter and Brodie (2004a,b)
59 have determined stress exponents of $n \approx 3$ and $n = 1$ and have demonstrated grain
60 size sensitive flow in quartz. These n -values are lower than previous n -values of $n =$
61 4 determined by Paterson and Luan (1990) and Luan and Paterson (1992) for
62 dislocation creep. Fukuda et al. (2018) and Richter et al. (2018) have determined n -
63 values of 1.7 to 1.9, respectively. These values were partly interpreted as a
64 combination of dislocation and diffusion creep mechanisms. As the experiments of

65 Kronenberg and Tullis (1987) have been carried out using fine grained novaculite,
66 and as this material has also been used in the experiments by Fukuda et al. (2018),
67 it appears likely that the pressure dependence of deformation has been determined
68 in material partially deformed by diffusion creep processes in the presence of H₂O.
69 The solubility of quartz in supercritical H₂O increases non-linearly with increasing
70 pressure (Manning, 1994, 2018), so that solution-precipitation processes may be
71 expected to be enhanced at high pressures. Diffusion creep in the presence of H₂O
72 will involve dissolution and precipitation and therefore is expected to be pressure
73 dependent. The pressure dependence of quartz rheology could therefore arise from
74 enhanced dissolution at higher pressures. For this reason, we have revisited the
75 pressure dependence of quartz deformation using a coarser grained quartzite (~200
76 µm grain size) as starting material in order to diminish the role of diffusion creep
77 processes and to test whether the dependence of quartz strength on pressure is the
78 same as in fine grained material and to study the processes of weakening in more
79 detail.

80 **2. Methods**

81 *2.1 Deformation experiments*

82 Coaxial shortening deformation experiments of natural quartzite (for the
83 characterization of the starting material see the results-section) have been performed
84 in two types of solid medium apparatus (a modified Griggs apparatus at University of
85 Tromsø, Norway and a new generation solid medium apparatus at ISTO, Orléans,
86 France). NaCl was used as the confining medium in both sets of experiments. The
87 preparation procedure followed for samples deformed in Orléans corresponds to the
88 one described by Précigout et al. (2018). For samples deformed in Tromsø,
89 assemblies differ in size (smaller diameter and length) and use a single
90 thermocouple instead of two.

91 Cylindrical samples (diameter 6.35 mm for samples in the conventional Øyggs
92 apparatus in Tromsø and 8 mm for the new rig in Orléans) were cored from the
93 starting material (without any preferential orientation), with ends ground flat and
94 plane-parallel to ~ 0.001 mm tolerance. They were dried at 110°C for one day
95 (minimum), then weighed, wrapped with two layers of nickel foil (0.025 mm
96 thickness), inserted into platinum jacket (0.15 mm thickness) and weld-sealed after
97 addition of 0.1 wt.% of distilled water.

98 For deformation experiments at 2 GPa confining pressure, the sample assembly
99 was slightly modified. The top piston and top inner salt piece were separated into two
100 parts and a disc of compressed salt (of approximately 2.6 mm thickness and 13 mm
101 diameter) was inserted in between. In this way, the deformation column was able to
102 compact as P and T were increased to the final P-T conditions of the experiment
103 without applying much deviatoric stress on the sample when advancing the pistons.
104 Before this modification of the sample assembly, several experiments failed as the
105 hit-point was reached during the pumping stage and the sample started to deform
106 earlier than expected.

107 All deformation experiments have been performed to approximately 30% coaxial
108 shortening (total strain of samples is between ~ 26 and 33%, except for the high-
109 strain OR56 sample of $\sim 74\%$) at a temperature of 900°C and constant strain rate of
110 approximately 10^{-6} s^{-1} – corresponding to a constant displacement rate of 1.5×10^{-5}
111 $\text{mm}\cdot\text{s}^{-1}$ (Table 2). The strain rate of experiments in the rig at Orléans was slightly
112 lower (by $\sim 30\%$) than in the Tromsø rig. However, for a power law solid, this
113 difference in strain rate should lead to only a subtle difference in flow stress.
114 Confining pressures were 600, 700, 800, 1000, 1250, 1500 and 2000 MPa (Table 2).
115 In the new type of solid medium apparatus, the pressure is regulated by a hydraulic
116 pump and remains constant throughout the experiment, whereas in the conventional

117 Onygs apparatus, it is not regulated and typically increases towards the end of the
118 experiment (the increase is corrected in the mechanical record).

119 One sample (OR56) was deformed at 2000 MPa at a faster strain rate of $\sim 10^{-5} \text{ s}^{-1}$
120 ($1.5 \times 10^{-4} \text{ mm.s}^{-1}$) and shortened by 70%. As the hit point was reached during the
121 pumping phase, the strength of this sample could not be determined.

122 Two strain rate stepping experiments have been performed in order to determine
123 the n-exponent of the flow law. During these experiments, the pressure (2000 MPa
124 for OR68 and 800 MPa for OR79) and temperature (900°C) conditions were kept
125 constant but the strain rate was changed. For both experiments, the strain rate
126 sequence was $\sim 1 \times 10^{-5}$, 10^{-7} , 10^{-6} and 10^{-5} s^{-1} . The n-exponent was then defined for
127 each experiment as the slope between the log of the strain rates at the end of each
128 strain rate step and the log of the differential stresses calculated by linear regression.

129 Processing of the mechanical data was carried out with a MATLAB program (Pec
130 et al., 2016) adapted by J. Précigout following the routines of Heilbronner
131 (<https://micro.earth.unibas.ch>). Finite strain of the deformed samples was calculated
132 from mechanical record and from direct measurements of samples lengths before
133 and after the experiments.

134 After the experiments, all samples were cut through the centre with a diamond
135 saw (passing through the thermocouple positions) to obtain a longitudinal section
136 parallel to the sigma 1 direction. Thin (30 μm) and thick (90 and 150 μm) sections
137 have been prepared from the two parts.

138 *2.2 Cathodoluminescence*

139 Cathodoluminescence (CL) imaging has been carried out on samples using the
140 light microscope (LM) and the scanning electron microscope (SEM). LM-CL-images

141 of thin sections have been recorded at BRGM (Orléans) with an CL-CA cold cathode
142 stage at approximately 10-12 kV and 120-150 μ A under low-pressure Argon gas at
143 6.7 to 7.3 Pa. The image acquisition time was 3 to 4 s. SEM-CL-images have been
144 recorded at BRGM (Orléans) with EDAX-Pegasus system equipped with a TESCAN
145 CL-detector. Conditions of imaging were 5 to 15 kV and 17 to 20 mm working
146 distance. Prior to analysis, samples were coated with 20 nm of carbon. Additional
147 mosaic CL-images have been recorded at the University of Tromsø using a Gatan
148 Mono-CL-system on a Zeiss Merlin Compact SEM at 15 kV and 12.5 to 13.7 mm
149 working distance using a blue filter (380-515 nm). These images have been manually
150 segmented and processed using ImageJ software.

151 2.3 Bulk sample strain analysis from sand grain shapes

152 Cathodoluminescence and plane polarized light microscopy allow to identify the
153 original sand grains of the Tana quartzite and to distinguish them from the cement.
154 Light microscope (cross-polarized and cathodoluminescence) mosaic images of the
155 starting material and of samples deformed at different pressures have been manually
156 segmented to isolate original sand grains. These sand grains have been analysed
157 using the open-source *ImageJ* program to obtain statistics on grain parameters
158 (cross section area, shape, orientation) as described by Heilbronner and Barrett
159 (2013).

160 The sand grain size is expressed as the equivalent diameter (d_{eq}) calculated from
161 the area of grains (A) as $d_{eq} = 2 \times \sqrt{\frac{A}{\pi}}$. The fabric is expressed as the aspect ratio
162 (AR), the mean ratio between the long (a) and short (b) axes of the particles ($AR = \frac{a}{b}$)
163 and their orientation. The dataset has been analysed by the SURFOR method
164 described by Panozzo (1984) in *ImageJ* for a fabric and strain analysis.

166 Crystal orientations have been determined by electron backscatter diffraction
167 (EBSD) using a Nordlys detector and an Oxford Aztec system on a Zeiss Merlin
168 Compact FE-SEM at the University of Tromsø using a 70° tilt angle, 20 kV
169 acceleration voltage, and 9 nA probe current. An indexing quote of 75-85% has been
170 achieved on 4 nm carbon coated thin sections. Post-processing was performed using
171 the MTEX v.5.2.8 program package by Bachmann et al. (2010). Orientation maps
172 were recalculated using the 6/mmm system (hexagonal) in order to avoid displaying
173 Dauphiné twin boundaries.

174 2.5 Fourier Transform Infrared (FTIR) Spectroscopy

175 Double-polished thick sections of 150 and 90 μm have been prepared from the
176 starting material and Fourier transform infrared spectroscopy (FTIR) analysis has
177 been performed at ISTO (Orléans) with Nicolet 6700 (Continuum, Thermoscientific)
178 spectrometer and OMNIC (version 8) acquisition software.

179 The spectra were acquired on grain interiors, grain boundaries, and cement with
180 64 and 128 scans and a resolution of 4 cm^{-1} for a range of wave numbers from 5500
181 to 1500 cm^{-1} . A window with $40\times 40\text{ }\mu\text{m}$ for interior of grains and with $20\times 50\text{ }\mu\text{m}$ was
182 used for grain boundary measurements (window shape and orientation was adapted
183 to the boundaries). The background was recorded for the CaF_2 window carrying the
184 sample and subtracted from the measured spectra. Water contents were calculated
185 using the Beer-Lambert law and the Paterson (1982) calibration.

186 2.6 Water fugacity calculations

187 Assuming that during the experiments the H_2O pressure approximatively equals
188 the confining pressure, the water fugacity ($f_{\text{H}_2\text{O}}$) can be calculated using only two pa-
189 rameters: the temperature and the pressure. The water fugacity has been computed

190 for all experimental conditions from Tony Withers' fugacity calculator (available at:
191 <https://www.esci.umn.edu/people/researchers/withe012/fugacity.htm>) based on the
192 Pitzer and Sterner (1994) equation of state for water.

193 **3. Results**

194 *3.1 Starting material*

195 For the starting material, a very pure natural quartzite from the ELKEM quarry in
196 Austertana, Northern Norway (N70°28'39.6'', E28°32'30.1'') has been used. The
197 rock samples come from the top part (~40 m) of the Gamafjell formation. This
198 sequence of late Precambrian age is approximately 300 m thick and its top part is
199 composed of grey to white quartzite (Pevik, 2015). The uppermost part of the
200 formation is described as very pure (> 99% of silica), and used by the aluminium,
201 silicon, and ferrosilicon industry (Aasly et al., 2007). Chemical analysis (from ICP-
202 EOS) published in Pevik (2015) indicate major oxide values (apart from SiO₂) of
203 3547 ± 1083 ppm Al₂O₃, 441 ± 365 ppm Fe₂O₃, and 207 ± 37 ppm TiO₂.

204 The Tana quartzite underwent high grade diagenesis to very low grade
205 metamorphic conditions and is weakly deformed in a large open antiform (Pevik,
206 2015). However, no internal deformation on the micro-scale, no schistosity, and no
207 lineation have been identified in the sampled rock. The blocks of the starting material
208 collected were not oriented. The quartzite is composed of quartz grains and
209 crystalline authigenic SiO₂ cement (99%, Fig. 1a) and very few accessory minerals
210 (< 1%) such as sheet silicates (sericite, pyrophyllite, kaolinite), iron oxides (hematite),
211 zircons, apatite, xenotime, monazite, rutile, and very rare feldspars. Due to filling of
212 the pore space by authigenic SiO₂ cement, no visible porosity was detected in the
213 light microscope or SEM.

214 Microstructural analysis and CL-imaging show that the quartz grains forming the

215 Tana quartzite are composed of (1) cores of equant and rounded detrital quartz sand
216 grains, with various CL-colours and -intensity, and (2) a non- or dark-luminescent
217 cement between the grains (Fig. 1c,d). The cement is in crystallographic continuity
218 with the sand grains on which it grows epitaxially (Fig. 1a). Grains appear
219 undeformed as they do not show any undulatory extinction, except for rare sand
220 grains showing inherited recrystallized microstructures. A few pressure-solution
221 contacts due to burial of the sediment are sometimes observed.

222 The size distribution of quartz grains composing the quartzite was obtained by
223 image analysis using both polarized light and light microscopy (LM)-CL-images. The
224 mean grain size is 204 μm for quartz grains and 186 μm for original sand grains
225 (Table 1). The quartz grain sizes are larger than those of sand grains because they
226 include the surrounding cement. The calculated mean aspect ratio (AR) is 1.56 for
227 quartz grains and 1.55 for sand grains, indicating that grains are somewhat
228 elongated. However, no preferred orientation of the long axes of the grains can be
229 detected. For this reason, samples have been cored without reference to any specific
230 orientation.

231 Electron Backscatter Diffraction (EBSD) measurements of grains from starting
232 material Tana quartzite (one point per grain, $n=500$) confirm a random fabric (Fig. 1b,
233 with $J=1.33$ and $M=0.027$), close to a random distribution (Bunge, 1982; Skemer et
234 al., 2005). The dislocation density of the material was characterized by transmission
235 electron microscopy (TEM) as $6 \times 10^{12} \text{ m}^{-2}$, which is a typical, low dislocation density
236 of relatively undeformed natural silicates (McLaren, 2005).

237 The mean water content calculated is $1659 \text{ H}/10^6 \text{ Si}$ for grain interiors and 2120
238 $\text{H}/10^6 \text{ Si}$ for grain boundaries.

240 3.2.1 Stress strain curves

241 The samples show a systematic decrease in strength with increasing confining
242 pressure (Fig. 2): the maximum final differential stress is nearly 600 MPa for a
243 sample deformed at 600 MPa confining pressure, whereas for the sample deformed
244 at 2000 MPa it is ~ 100 MPa. This behaviour is reproducible for the two different
245 apparatus (considering a ± 30 MPa accuracy of the solid medium apparatus;
246 Holyoke and Kronenberg, 2010) used for a confining pressure of 1000 MPa (samples
247 546LN and OR32; the strain rate is slightly lower in OR32) whereas for lower
248 pressure at 600 MPa, the sample deformed in Orléans (OR60) is slightly stronger
249 than the one in Tromsø (542LN), despite the slightly slower strain rate.

250 3.2.2 Strain rate stepping experiments

251 Two strain rate stepping experiments were performed at high (OR68, 2000 MPa)
252 and low (OR79, 800 MPa) pressures to determine the n-value, or the stress
253 exponent, of the flow law. Both experiments were conducted at 900°C with 0.1 wt.%
254 water added and with a strain rate sequence of $\sim 10^{-5}$, $\sim 10^{-6}$, $\sim 10^{-7}$ then again $\sim 10^{-5}$
255 s^{-1} . The stress-strain-curves are presented in Fig. 3a and flow stresses for each step
256 are reported in Table 3.

257 The initial step at $\sim 10^{-5} \text{ s}^{-1}$ has been repeated at the end of the experiments for a
258 test of reproducibility. The flow stresses associated to that rate are systematically
259 higher during the final step and steady state has not really been reached for the
260 lower confining pressure experiment. For the steps at $\sim 10^{-7} \text{ s}^{-1}$, both samples show
261 an unstable and variable behaviour, probably due to the low sample strength, so that
262 possibly some friction effects at the pistons start to play a role. In addition, at such
263 low strain rates the initial “friction” of the run-in curve is partially recovered, so that
264 the recorded stresses may be too low (see explanation of this effect in Tarantola et

265 al., 2012, appendix). In the next generation Sanchez apparatus, very low or low is
266 injected by the hydraulic pump (0.0007 mL/min) in order to obtain this strain rate, this
267 variation may partially reflect changes in the ambient conditions (daily variations
268 recorded for the force, influenced by room temperature or cooling temperature
269 variations).

270 The n-exponent is defined as the slope of the linear regression in the log-log plot
271 of the flow stresses vs. strain rate (Fig. 3b). For the low pressure experiment (OR79,
272 800 MPa), $n \sim 1.42$ is obtained, and for the high pressure one (OR68, 2000 MPa),
273 $n \sim 1.40$. Given the uncertainties of the stress determination in the solid medium
274 apparatus, these n-values are identical. If the slowest strain rate steps are omitted as
275 somewhat less reliable (see above), the resulting n-values are 2.33 for 2000 MPa
276 and 1.96 for 800 MPa confining pressure.

277 3.3 Microstructures

278 3.3.1 Light microscopy

279 The local strain distribution in all samples is inhomogeneous. Typically, the centre
280 and/or bottom parts of the samples are more strongly deformed (Fig. 4). The
281 partitioning of deformation typically is detected by more elongated grain shapes in
282 the higher strained regions (Fig. 4b). The greater elongation of individual quartz
283 grains usually is accompanied by an increase in the amount of recrystallized
284 material. Original quartz grains in deformed samples show evidence for plastic
285 deformation, such as undulatory extinction, deformation lamellae and, in some
286 places, development of subgrains (observed in the LM; Fig. 4c). Some of the
287 progressive subgrain rotation leads to the formation of core-mantle structures (Fig.
288 4b,c).

289 This strain gradient is slightly more pronounced for samples deformed in the

290 conventional Ohggs apparatus at Homsø (where more of the deformation is
291 localized at the lower part of the samples) than for those deformed in the new
292 apparatus in Orléans (where more of the deformation is located in the central part of
293 the sample). This type of strain localisation is common in samples deformed in the
294 solid medium apparatus (e.g., Heilbronner, 2002; Heilbronner and Tullis, 2002;
295 Stünitz et al., 2017) and is related to the temperature gradient in the sample. The
296 thermocouple position indicates the highest temperature of the sample ($< 90^{\circ}\text{C}$
297 temperature difference between sample ends and the hot zone = thermocouple
298 position) and this region typically corresponds to the higher strain regions.

299 3.3.2 Cathodoluminescence

300 SEM-CL and LM-CL images show that in all deformed samples the original sand
301 grains can still be identified by the same variation of luminescence and tints as in the
302 starting material (Figs. 1 & 5). The sand grains in the more highly deformed parts of
303 the sample show a more elongated shape with the long axis at a large angle or
304 normal to the shortening direction. In the cemented area between the original sand
305 grains, the darker luminescent cement is clearly observable. However, in the
306 deformed samples, a new material with a bright luminescence appears in CL-images
307 (Figs. 5 & 6). This bright luminescence material invariably has a blue colour, so that
308 a blue filter was used in SEM-CL images to enhance its presence. The blue
309 luminescence is not short-lived but permanent.

310 3.3.2.1 Morphology of the bright luminescent material

311 The bright luminescence material in deformed samples is often concentrated in
312 the boundary regions of grains, so that these bright regions appear predominantly in
313 the cement at the grain boundaries of quartz grains. In some cases the bright
314 luminescing material cuts across original sand grains (Fig. 6a,b). In the low strain
315 parts of the samples, the brightly luminescing zones follow a clear crack morphology

316 (Figs. 5 & 6). The bright luminescent material occurs in the cracks that cut through
317 both, sand grains and cement. This is observed in samples deformed at low
318 confining pressure (e.g., OR42, 800 MPa, Fig. 6a) and at higher confining pressure
319 (546LN, 1000 MPa, Fig. 6b). In samples deformed at low confining pressure, cracks
320 are subparallel to the loading direction and appear to have been dilatant, mode I
321 cracks, before new quartz material has filled the cracks. The inner parts of these
322 cracks can be filled with non-luminescent material (Fig. 6a). From the boundaries of
323 the healed mode I cracks, very thin cracks extend perpendicular to the mode I
324 cracks, i.e., in an orientation typical for unloading cracks (Fig. 6a). The appearance
325 of such cracks has first been observed in samples deformed in the Griggs-type
326 apparatus by Fitz Gerald et al. (1991), and these features have been termed "step-
327 ladder cracks". In all deformed samples, many thin cracks with bright luminescence
328 in a direction perpendicular to the shortening direction extend from grain boundaries
329 and cracked regions and have formed as unloading cracks during decompression of
330 the samples (e.g., Fig. 6b).

331 In samples deformed at higher confining pressure, cracks tend to be thinner, more
332 irregular, and are distributed more pervasively across the samples (Fig. 5e,f). They
333 often (but not necessarily) follow the grain boundaries (intergranular cracks). For all
334 the cracks in the samples, no or very little displacement has been observed along
335 the cracks.

336 The brightly luminescing material sometimes forms overgrowths with crystal faces
337 on pre-existing large grains or filling intergranular spaces (Fig. 6c,d). EBSD maps
338 performed on these areas indicate that these faceted overgrowths are in
339 crystallographic continuity with the parent grain. The faceted crystals can be
340 surrounded by non-luminescent material in pore spaces (Fig. 6c,d).

341 Larger regions of bright luminescent material consist of aggregates of many small
342 new grains (Fig. 6d). Many of the small grains are brightly luminescent throughout
343 but others have a darker luminescent core with a bright rim of variable thickness (Fig.
344 6d). Comparison between bright luminescent zones and the corresponding regions
345 under crossed polarizers indicate that all of these regions consist of small grains,
346 luminescing in blue, but not all luminescent regions consist of small grains. The
347 amount of brightly luminescent material increases substantially with increasing strain
348 (see also below). In a sample deformed to 74% strain (OR56) the original grains are
349 strongly elongated and are embedded in a matrix of 30% luminescent material (Figs.
350 5f & 12).

351 3.3.2.2 *Evolution of luminescent regions as a function of pressure and sample* 352 *strain*

353 For four samples (546LN, OR42, OR57 and OR56), SEM-CL longitudinal
354 transects have been recorded from the top to the bottom (example for OR57 sample
355 on Fig. 7). All transects were segmented manually in order to separate the original
356 sand grains and cement from the bright luminescent material. The segmented
357 images were then processed with the *ImageJ* software in order to quantify the
358 amount of bright luminescence regions in samples.

359 Domains with higher finite strain show a higher proportion of brightly luminescent
360 areas. This relationship can be observed at the scale of a given sample, between the
361 top – relatively undeformed part – and the bottom part – where deformation is much
362 more intense (OR62, Figs. 5e & 8a). The relationship can also be observed in
363 samples deformed to different amounts of total strain (e.g, OR56; Fig. 5f). There is a
364 relationship between the amount of brightly luminescent material and confining
365 pressure demonstrated for the three samples strained up to 30% (OR42, 546LN and
366 OR57). The amount of brightly luminescent material increases in the middle to

367 bottom part of the samples (more deformed regions, Fig. 6a): 9.66% for sample
368 OR42 (800 MPa), 10.72% for sample 546LN (1000 MPa), 15.08% for sample OR57
369 (2000 MPa; Fig. 7). Thus, there is a trend of increasing amount of brightly
370 luminescent material with increasing confining pressure and with strain (Fig. 8b).

371 *3.4 Strain analysis from fabric and grain shapes*

372 The starting material and samples deformed at 700, 1000, 1500 and 2000 MPa
373 confining pressure have been studied for their grain shapes and fabric by image
374 analysis. The goal of the analysis was to compare the bulk sample strain determined
375 from the mechanical record and from measuring sample lengths with an analysis
376 based on strain of individual quartz grains. Such an analysis is difficult in normal
377 quartz grain aggregates because the regions of dynamic recrystallization make it
378 difficult to identify original grain shapes as passive markers. The outlines of original
379 sand grains in the Tana quartzite represent true strain markers for the deformed
380 samples, because dynamic recrystallization typically affects the grain boundary
381 region first (e.g. formation of “core and mantle” structures), i.e. the cement regions.
382 However, the sand grain outlines are located inside the original quartz grains and are
383 only rarely affected by the bright luminescence regions. Furthermore, they present
384 passive markers because the cement overgrowth is in crystallographic continuity with
385 the original sand grains. In addition, the orientation of long axes of the sand grains
386 and their fabric are more or less random in the starting material (Table 1).

387 An example of the segmentation of the OR62 sample (2000 MPa) is shown in Fig.
388 9. Sand grains are manually separated from surrounding cement in LM-CL-images.
389 In this way, only the original sand grains and their internal plastic deformation are
390 considered for this strain analysis.

391 Sand grain size and parameters calculated from the analysis of mosaic LM

392 cathodoluminescence images are presented in Table 4. The number of analysed
393 grains varies with the grain sizes (sample size for 546LN is smaller). The equivalent
394 diameter of sand grains varies with the layers in the starting material and is not a
395 function of deformation. The aspect ratio of individual grains increases for deformed
396 samples (from 1.55 to 2.05) in comparison to the starting material. No correlation
397 emerges between confining pressures and equivalent diameters or aspect ratios
398 neither with sample bulk strain (calculated or measured).

399 The SURFOR program facilitates the calculation of the sample strain/fabric
400 anisotropy from the particle outlines of the starting material and deformed samples.
401 The results are presented in Table 5 and shown in Fig. 10. The difference between
402 the minimum and maximum of the projection curves corresponds to the global strain
403 value (from 0 to 1). The angular difference between the maximal and minimal
404 position of the projection curve should be 90° (corresponds to the angle between
405 shortening and extension direction), and the value of the minimum corresponds to
406 the shortening direction.

407 For the starting material (TQ) the minimum of the curve is 0.965 for $\alpha=70^\circ$,
408 indicating a very slight flattening of the grains. However, as the studied thin section
409 was not oriented in a particular way and the cores for experimental samples were not
410 made in the same orientation, this value indicates the general fabric anisotropy of the
411 starting material but does not correspond to the orientation of this material in the
412 apparatus. Yet, we should consider the $\pm 3.5\%$ anisotropy as a mean error for
413 strained samples.

414 For deformed samples, the bulk shortening for the grain fabric calculated by the
415 SURFOR analysis is between 22.9 and 37.2%. For the samples OR52, OR64 and
416 OR62 the values are very close to the ones calculated from mechanical data and

417 measured on thin sections and are within the error range ($\pm 0.5\%$). However, for
418 546LN, the shortening value is underestimated and overestimated for OR32
419 (difference up to $> 8\%$).

420 3.5 EBSD maps and misorientation calculations

421 Two regions were selected for detailed EBSD analysis: (1) a low strain region with
422 limited recrystallization and formation of discrete luminescence in response to
423 cracking (546LN), and (2) a high strain region affected by more extensive
424 recrystallization/luminescent material (OR56).

425 In region (1) the cracks are visible in the SEM-CL image, cutting through original
426 quartz sand grains as well as cement (Fig. 11a). The corresponding EBSD map of
427 this region shows small new grains (clasts) that make high angle boundaries with the
428 larger quartz grains in the traces of the cracks. In addition, some low angle
429 boundaries also separate the small clasts from the host quartz grains (Fig. 11b). The
430 size of the clasts (new grains) can be as small as $1\text{-}2\ \mu\text{m}$ and as large as $\sim 10\ \mu\text{m}$
431 (Fig. 13). Low angle new grains (in Fig. 13 marked as “subgrains”) and the high
432 angle new grains (in Fig. 13 marked as “recrystallized grains”) do not show different
433 size distributions, only high angle new grains are more frequent (Fig. 13). On the
434 scale of the EBSD maps, the smaller and larger clasts all have more or less rounded
435 shape (Fig. 6c,d). This is the case in light microscope images, too (Fig. 4). The clasts
436 typically have a bright blue luminescence colour. The clasts with low angle
437 boundaries ($< 10^\circ$) only show a weakly preferred misorientation axis in $[0001]$,
438 whereas the larger angle boundaries are misoriented with axes in $[0001]$ and $[-12-10]$.

439 In the high strain region (2), the original quartz grains appear bright in the SEM-CL
440 image, and the recrystallized matrix is medium grey (blue luminescence; Fig. 12).
441 Some relict parts of original quartz grains are present as porphyroclasts with bright

442 luminescence surrounded by a matrix of recrystallized grains (separated mostly with
443 high angle boundaries). The corresponding EBSD map shows a large number of
444 recrystallized grains of 1-2 μm size with high angle boundaries in the matrix (Fig. 13).
445 The two large relict quartz grains (labelled 1744 and 3542 in Fig. 12) show a number
446 of subgrains with low angle boundaries ($< 10^\circ$ misorientation from the large quartz
447 porphyroclast) forming regions of subgrains between the porphyroclast and the
448 recrystallized matrix. The subgrains do not show different luminescence from their
449 host grains. The two large grains show different distributions of misorientation axes
450 for their subgrains: [0001] (in 1744) and no preferred axis (in 3542). The high angle
451 grain boundary misorientations (Fig. 12c,d) have rotation axes of [1-100] (in 3542)
452 and axes between [1-100] and [-12-10] (in 1744). The subgrain sizes are in the
453 same range as the sizes of small recrystallized grains (Fig. 13).

454 The sizes of relict grains do not differ between the two microstructures (Fig. 13
455 and Table 6). Relict grains are those grains that are located in a matrix of
456 recrystallized grains. The original large porphyroclasts of the starting material
457 typically are too large to be included completely in the EBSD maps. They are cut off
458 at the margins of the map and therefore are not counted. The proportion of subgrains
459 and recrystallized grains is much higher in the high strain sample OR56 than in the
460 lower strain sample 546LN (Fig. 13).

461 **4. Discussion**

462 *4.1 Deformation processes*

463 We observe two deformation processes that operate in all deformed samples:
464 Cracking and crystal plastic deformation. Crystal plastic deformation is visually
465 dominant in the microstructures, and the fact that the bulk sample strain can be
466 calculated from the particle strain of original sand grains within a few percent error
467 (Fig. 10, Tables 2 & 5) documents that most of the bulk shortening of the samples is

468 produced by crystal plastic deformation of individual original quartz grains. The
469 undulatory extinction, deformation lamellae, and progressive subgrain rotation (Figs.
470 4 & 12) observed in the quartz grains are consistent with this observation. Thus, the
471 dominant process of deformation in all samples is crystal plastic deformation, i.e.
472 dislocation creep, as it has been documented previously for quartz under these P-,
473 T-, strain rate conditions (e.g., Griggs, 1967; Jaoul et al., 1984; Kronenberg and
474 Tullis, 1984; Hirth and Tullis, 1992).

475 Despite the dominance of plasticity, cracking takes place in all samples (Figs. 5 &
476 6). Even though the crack morphology changes with confining pressure, there is one
477 feature that is common to all observed cracking: the cracks accommodate very little
478 displacement, so that the cracks do not contribute significantly to the finite strain.
479 Furthermore, the highest stresses attained in these experiments are all (except
480 sample OR60) below the Goetze criterion ($\Delta\sigma < P_{\text{conf}}$). This criterion defines the
481 upper differential stress limit of plastic or viscous deformation (brittle-plastic
482 transition; Kohlstedt et al., 1995). In the presence of a pore fluid, this criterion has to
483 be considered with some care (Hirth and Beeler, 2015; Beeler et al., 2015). The
484 effect of pore pressure at high pressure and temperature conditions and small
485 amounts of pore fluid is poorly investigated, but recent results by Okazaki et al.
486 (2021) indicate that at the porosity of our experiments (0.12 vol%, using the density
487 of H₂O from data by Larrieu and Ayers (1997)), the potentially expected reduction of
488 differential stress by pore pressure effects should be in the range of experimental
489 error (± 30 MPa; Holyoke and Kronenberg, 2010). Thus, the effective pressure
490 coefficient α in $\sigma_{\text{eff}} = \sigma_n - \alpha P$ (see Beeler et al., 2015) should be close to zero, so that
491 dominant viscous deformation can be concluded from the mechanical data for all of
492 the samples, consistent with the dominant deformation mechanism in the
493 microstructures.

494 The observed mode I cracks (Fig. 6a) have geometries typical of those formed at
495 low confining pressures (P_{conf}), (e.g. Paterson and Wong, 2005) and their occurrence
496 in samples deformed at the lowest P_{conf} is not surprising. We expect that such cracks
497 in the higher pressure samples have formed during early stages of the experiments,
498 by processes described previously in quartz experiments in the solid medium
499 apparatus (Fitz Gerald et al., 1991; Chernak et al., 2009; Tarantola et al., 2010;
500 Stünitz et al., 2017). These stepladder cracks (Fig. 6a,b) form as the result of a
501 sequence of initial cracking and subsequent crack healing, during which dislocations
502 are produced, followed by the glide of some of these dislocations. As a
503 consequence, there is a zone of plastically shortened material that forms
504 immediately adjacent to the crack. During unloading of the sample at the end of the
505 experiment this zone expands and develops unloading cracks (Fitz Gerald et al.,
506 1991; Stünitz et al., 2003, 2017). In this way the stepladder cracks document the
507 initiation of crystal plastic deformation in which local brittle processes and healing of
508 cracks play an important role. The CL observations document that cracking is a
509 ubiquitous feature during the dominant plastic deformation of quartz at high
510 temperatures of 900°C. At higher confining pressures cracks tend to have a different
511 geometry, but the interaction of cracking, crack healing, and plastic deformation is
512 not expected to change. The microstructures also document that cracking without
513 major displacement and thus without major kinematic contribution to strain
514 accommodation may be common at high temperatures when the sample strain is
515 dominantly accommodated by plastic mechanisms and flow stresses are low,
516 especially at high confining pressure (Fig. 2).

517 *4.2 Recrystallization processes*

518 Recrystallized material in all samples is marked by blue luminescence. The blue
519 luminescence colour is caused by a re-working (recrystallization) of quartz involving

520 an interaction with the aqueous fluid facilitating an exchange of trace elements of
521 producing defects during crystal growth (e.g. Ramseyer et al., 1988; Götze et al.,
522 2001). The blue luminescence is and has been attributed to Ti-incorporation into
523 quartz (Spear and Wark, 2009; Bestmann and Pennacchioni, 2015). It is unclear how
524 Ti-incorporation could have been achieved in the deformed samples in our
525 experiments, because a major Ti-source is lacking (although minute amounts of Ti-
526 phases (rutile) are present in the starting material) and Ti-incorporation during
527 recrystallization has been demonstrated to be slow and not producing homogeneous
528 equilibrium compositions easily (Negrini et al., 2014). A detailed analysis of the trace
529 element exchange that causes the luminescence was not attempted here because it
530 is beyond the scope of this study. However, as a potential origin of luminescence by
531 deformation-induced defects is very unlikely – these defects in quartz typically show
532 red luminescence colours (Hamers et al., 2016, 2017), and this type of luminescence
533 disappears after some electron beam irradiation (Bestmann, pers. Comm.) – it is
534 inferred that luminescence is caused by an interaction of the quartz with an aqueous
535 fluid during the reconstitution of the material. Therefore, it is concluded that the
536 luminescence observed in our samples is the result of exchange of trace elements
537 with a fluid during recrystallization of quartz (facilitated by boundary migration). This
538 makes luminescence a useful tool to trace recrystallized material in the deformed
539 samples.

540 Some of the recrystallization takes place by progressive subgrain rotation as
541 documented by EBSD maps (Figs. 11 & 12). Subgrains with misorientation angles of
542 $< 10^\circ$ are dominantly rotated around the [c]-axis. Such rotations can be produced by
543 tilt walls made up of edge dislocations in the prism planes with $\langle a \rangle$ Burgers vectors
544 or by twist boundaries in the basal plane made up of screw dislocations with $\langle a \rangle$
545 Burgers vectors (e.g., Trépiéd et al., 1980; Kilian and Heilbronner, 2017). Thus, this

546 constitutes evidence for prism $\langle a \rangle$ or basal $\langle a \rangle$ slip. For misorientations $> 10^\circ$,
547 rotation axes are parallel to $[-1100]$ or between $[-1100]$ and $[-12-10]$, consistent with
548 basal $\langle a \rangle$ or combined basal $\langle a \rangle$ and prism $\langle c \rangle$ slip. However, it is difficult to infer
549 slip systems accurately for larger misorientation angles, because misorientations
550 may partially be produced by grain boundary sliding processes once high angle
551 boundaries are established. The microstructures of subgrain boundaries within
552 original quartz porphyroclasts and the immediately adjacent grains with high angle
553 boundaries exhibit core-mantle structures (Fig. 12) and indicate progressive subgrain
554 rotation as the dominant recrystallization mechanism for such grains. Subgrains with
555 low angle boundaries and recrystallized grains with high angle boundaries do not
556 differ systematically in size (Fig. 13). The P-, T-, strain rate conditions of deformation
557 of the samples are those of regime 2 creep according to Hirth and Tullis (1992),
558 where rotation recrystallization is dominant. In these microstructures, the
559 luminescence of the porphyroclasts and their subgrains does not change, so that
560 non-recrystallized parts of porphyroclasts with subgrains still maintain the original
561 luminescence of the porphyroclasts (Fig. 12a). This observation is consistent with the
562 process of fluid exchange discussed by Negrini et al. (2014): formation of subgrain
563 boundaries is a climb process, which does not *a priori* involve any grain boundary
564 mobility and thus no interaction or exchange with a fluid phase. Once high angle
565 boundaries are established, grain boundary mobility may lead to exchange with a
566 fluid, producing different luminescence colours of these recrystallized grains.

567 A completely different process can form new grains in the deformed samples, too.
568 Local cracking produces small new grains, especially at grain boundaries and in local
569 cracks cutting through original quartz grains (Figs. 5, 6 & 11). Some new grains show
570 high angle misorientation relationships, whereas others show low angle relationships
571 along the same zones of cracks (Fig. 11). The CL images indicate that in some

572 cases, inner parts of clasts can still show the original luminescence of old grains,
573 whereas rims and small grains nearby show the blue luminescence typical of
574 reconstituted material (Figs. 6d, 11, 16). From these microstructures, it is inferred
575 that the small clasts in cracks have mobile boundaries that migrate and can produce
576 a reconstitution (recrystallization) of the quartz and exchange trace elements to
577 produce the different luminescence. Local grain boundary migration processes have
578 been inferred in previous studies (Stipp et al., 2002a, 2002b), where the migration
579 process is inferred to be the first step. A second type of process is subsequently
580 required to produce isolated new grains, because the local migration itself cannot
581 isolate small new grains. This second step can be subgrain formation and/or local
582 cracking (Stipp et al., 2002a, 2002b). In this study, we can observe the dominance of
583 cracking in certain locations of the sample, where new grains form (Figs. 4 & 5). The
584 sequence in this study is reversed: the cracking occurs first, followed by boundary
585 migration to exchange with the fluid. It is proposed here that cracking and local
586 boundary migration operate to produce microstructures that are consistent with what
587 is termed “bulging recrystallization” in the literature (e.g., Bailey and Hirsch, 1962;
588 Stipp et al., 2002a, 2002b; Stipp and Kunze, 2008). Local bulging may occur in these
589 samples, too, so that probably not all of the bulging recrystallization microstructures
590 are induced by cracking.

591 The brittle origin of new grains in quartz and other silicates during plastic
592 deformation has been described by van Daalen et al. (1999) in natural rocks, and by
593 Stünitz et al. (2003, 2017) and Vernooij et al. (2006) in experiments. The CL-
594 microstructures of these deformed samples indicate that the original clasts become
595 modified by grain boundary migration processes after their initial formation by
596 cracking. The misorientation of the small clasts with low angle boundaries shows a
597 weak preference of c-axis rotation, whereas higher angle boundaries can be

599 Grains with blue luminescence and faceted crystal shapes in open pore spaces
600 tend to show oriented overgrowth in crystallographic continuity with original
601 porphyroclasts (Figs. 6c & 11b) and have been described by Palazzin et al. (2018)
602 for dilatant sites that act as small local reservoirs of fluids. These microstructures
603 testify to the fast precipitation in dilatant sites and to the fact that there is excess H_2O
604 in these samples (so that $a_{\text{H}_2\text{O}} = 1$). Thus, the samples deformed at different
605 confining pressures show two types of recrystallization that takes place during
606 deformation: (1) progressive subgrain rotation, and (2) crack-related local grain
607 boundary migration that appears to be a type of bulging recrystallization. Both
608 operate at the same time in samples, although the geometry of some cracks
609 indicates an early origin of these.

610 *4.3 Dislocation creep and stress exponent*

611 From the conclusion of crystal plasticity, the operation of climb and dislocation
612 glide are dominant deformation mechanisms, an n -value for the stress exponent of n
613 = 3 to 5 would be expected for climb controlled creep (e.g., Paterson, 2012). Our
614 strain rate stepping experiments have yielded n -values of ~ 1.4 or ~ 2 , depending on
615 whether the slowest strain rate steps are considered or not. The variance of these
616 values and the uncertainty of the slowest strain rate steps require more detailed
617 investigation and a better data base to determine the stress exponent more
618 accurately. However, the present determination of $n \sim 2$ suggests values of $n < 3$ and
619 is consistent with observations of Fukuda et al. (2018) and Richter et al. (2018) in
620 quartz aggregates. Both research groups have concluded a contribution of diffusion
621 creep (including dissolution precipitation creep) to the viscous deformation of quartz.
622 Richter et al. (2018) have observed weaker preferred orientation of quartz in fine
623 grained aggregates, and the $n \sim 2$ values are explained by a combination of

624 dislocation and diffusion creep deformation in their samples. The values obtained
625 here are lower than $n = 3$ to 5 , too, and therefore inconsistent with typical n -values
626 for pure dislocation creep (Fig. 3b).

627 The starting material in the samples of this study is coarse grained, so that
628 diffusion creep in the starting material is unlikely. However, some of the recrystallized
629 material (in particular the cracked material in bulging-type microstructures) is fine
630 grained, and some diffusion creep in the recrystallized material is conceivable. In
631 addition, extensive exchange with aqueous fluid in the recrystallized material is
632 observed in our samples, so that diffusive mass transfer processes are evident.
633 Thus, it is inferred that the low n -values of $n \sim 2$ in our samples may also be explained
634 by a combination of dislocation and diffusion creep processes. A potential
635 explanation of dislocation accommodated grain boundary sliding (disGBS), as it is
636 inferred in olivine (e.g., Hansen et al., 2012) is unlikely, because it would require the
637 whole material to consist of fine grain sizes.

638 As diffusion creep is grain size dependent, its contribution to the deformation
639 process is expected to increase with an increase of fine grained material or decrease
640 with grain growth. In most of our samples, steady state deformation is observed (Fig.
641 2), as it is typical for the dislocation creep regime 2 as defined by Hirth and Tullis
642 (1992). This observation suggests that an increase of recrystallized material does not
643 increase the contribution of diffusion creep. The reason for this may be that grain
644 growth (= migration processes) of very small grains produced by cracking takes
645 these grains out of the diffusion creep field (producing an equilibrium recrystallized
646 grain size). Continued microcracking may produce new very small grains, which in
647 turn may grow. These processes appear to be in a steady state to produce steady
648 state deformation. However, it is premature to speculate further on this aspect, and
649 more research is required to investigate the relationship between cracking and

650 recrystallization processes in more detail.

651 4.4 Effect of H₂O and pressure

652 The progressive lowering of the flow stress with increasing confining pressure in
653 our samples is consistent with the initial observations by Kronenberg and Tullis
654 (1984) and Mainprice and Paterson (1984). When the stresses (taken at 15%
655 shortening, where all samples reach more or less steady state flow stress) are
656 plotted as a function of the confining pressures, a power law relationship between
657 the flow stress and the confining pressure of the form $\sigma_{diff} = 505522 P_c^{-1.113} \text{ MPa}$ is
658 found (Fig. 14), similar to that of Kronenberg and Tullis (1984). However, in this
659 study, a coarse grained quartzite instead of fine grained novaculite was used (as in
660 Kronenberg and Tullis, 1984), confirming that the process of pressure-dependent
661 weakening in quartz is not dependent on grain size of the starting material.

662 Kohlstedt et al. (1995) proposed that the pressure dependence of the rheology
663 should be expressed as a fugacity term with exponent m in the quartz flow law. The
664 log-log plot of flow stresses vs. fugacity (Fig. 15) allows a fit of the $r = m/n$ value,
665 which is -0.46 for our samples. The plot in Fig. 15 shows other data from the
666 literature together with our data, but the curve fit is only shown for data of this study.
667 The $r = m/n$ value is similar to that of Post et al. (1996) (-0.47), Kronenberg and Tullis
668 (1984) (-0.5, as fitted by Post et al., 1996), Chernak et al. (2009) (-0.40), and of
669 Holyoke and Kronenberg (2013) (-0.63, for their quartzite). It should be noted that
670 experiments by Kronenberg and Tullis (1984) and Holyoke and Kronenberg (2013)
671 were performed at 800°C, those of Post et al. (1996) and Chernak et al. (2009) at
672 900°C and 1.5 GPa. A linear regression to all existing data yields almost the same
673 slope as our data (0.458 vs. 0.460), but with a much lower correlation coefficient
674 (0.71 vs. 0.93). This situation confirms the validity and applicability of our new data
675 set.

676 The exponent m for the fugacity depends on the n -value of the stress exponent. In
677 this study, a stress exponent of $n \sim 2$ is inferred, which would result in an m -value of
678 0.92, or $m \sim 1$. An m -value of $m=1$ has been determined by Fukuda et al. (2018) for
679 their n -value of 1.7, quite consistent with our results. If n -values closer to $n=4$ are
680 chosen, as determined by Paterson and Luan (1990) and Gleason and Tullis (1995)
681 and used in Hirth et al. (2001) and others, or $n=2.7$ (or $n \sim 3$, Rutter and Brodie,
682 2004), as proposed by Tokle et al. (2019), the m -value would be $m=1.84$ or 1.24.
683 However, the original m -value of 1 proposed by Kohlstedt et al. (1995) is consistent
684 with our results and those of Fukuda et al. (2018) for their m/n and n -values.

685 Lu and Jiang (2018) have proposed to correct the quartz flow law for pressure by
686 using an activation volume term. This correction would have the opposite effect as
687 the fugacity correction, and it is only meaningful to employ such a term once the
688 activation energy is precisely determined. The presently existing data base of Q -
689 values shows a large scatter (see compilation in, e.g., Richter et al., 2018), so that it
690 appears to be necessary to determine Q accurately as a first step, before an
691 activation volume term needs to be considered. We therefore do not consider the
692 activation volume here.

693 *4.5 What is the cause of sample weakening with increasing pressure?*

694 In previous studies of quartz deformation with the presence of H_2O the weakening
695 effect has been inferred as due to enhanced recrystallization or recovery (Tullis et
696 al., 1979; Tullis and Yund, 1989). Subgrain boundary formation is enhanced in
697 quartzites deformed with H_2O and grain boundary migration forms dislocation-free
698 grains during dynamic recrystallization. Both processes are faster at higher confining
699 pressures. Our results are consistent with this interpretation. The amount of
700 recrystallized material increases with increasing confining pressure (Fig. 8), and this
701 is the most obvious difference in the microstructures with increasing confining

702 pressure, apart from a different crack geometry. The recrystallization in our samples
703 involves grain boundary migration, which, in the presence of an aqueous fluid, can
704 be described as a process of solution and precipitation with a very short transport
705 distance of dissolved species across the boundary region. The solubility of SiO_2
706 increases non-linearly with increasing pressure (e.g., Manning, 1994, 2018), so that
707 enhanced boundary migration rates are likely with increasing pressure because of
708 enhanced solubility of quartz, provided that an efficient precipitation process can be
709 identified. The precipitation may be favoured at local dilatant sites which may form by
710 grain boundary sliding and in which precipitation has been observed or inferred
711 (Fusseis et al., 2009; Menegon et al., 2015; Okudaira et al., 2015; Précigout and
712 Stünitz, 2016, Précigout et al., 2017, 2019). In fine grained material, grain boundary
713 sliding is an important mechanism to accommodate shape changes of grains
714 induced by plastic deformation of grains (glide of dislocations) and to adjust for the
715 plastic strain incompatibilities as a consequence of an insufficient number of slip
716 systems in silicates (compared to metals). The low n -values (Fig. 3) in strain rate
717 stepping experiments are consistent with grain boundary sliding and diffusion creep
718 components of deformation. Grain boundary sliding and local dilatancy in the form of
719 cavitation is likely to occur in these aggregates and may cause immediate
720 oversaturation of the fluid and precipitation of quartz. Overgrowth of quartz seams on
721 quartz grains is observed in larger dilatant sites (Fig. 6c). Replacement of quartz
722 material during grain boundary migration is evident from the change of CL colours in
723 the recrystallized material, indicating boundary migration by dissolution, precipitation,
724 and exchange of elements with a fluid.

725 It has been pointed out above that once high angle boundaries are established,
726 the distinction of grains formed by progressive subgrain rotation and those produced
727 from initial cracking is possible (Pongrac et al., in prep.), but it is not easy, because

728 their size is similar and they all show bright luminescence. It is inferred that in this
729 material the weakening effect takes place as a consequence of increased confining
730 pressure. The inference that the pressure-dependent H₂O-weakening is caused by
731 grain boundary processes is supported by the observation by Holyoke and
732 Kronenberg (2013) that the pressure dependence of the flow stress in polycrystalline
733 aggregates is greater than in single crystals. Consequently, these authors have
734 attributed the weakening effect to recrystallization/recovery processes (Tullis and
735 Yund, 1989) at grain boundaries, too.

736 The plot in Fig. 15 suggests that the pressure effect of H₂O-weakening could be
737 greater at low pressure than at high pressures. A potentially greater m-value may be
738 caused by a change in n- or r-values in $m = r/n$. The determination of the stress
739 exponent is not precise enough at this stage to decide whether a constant n-value
740 would require an intrinsic effect of the H₂O fugacity or whether the potentially
741 changing pressure dependence of flow stress could be caused by a change in the
742 stress exponent n.

743 *4.6 Geological application*

744 The lowering of quartz flow stresses with increasing confining pressures that has
745 been documented since the study by Kronenberg and Tullis (1984) – also
746 documented in this study – suggests that in subduction channels at high pressure
747 the strength of quartz dominated lithologies is expected to be very low. Low stresses
748 for deformation in subduction zones have been inferred by Stöckhert et al. (1997,
749 1999), Stöckhert and Renner (1998), Stöckhert (2002) and Wassmann and Stöckhert
750 (2013), partly based on different deformation mechanisms. This study confirms that
751 even for dislocation creep, where stresses tend to be higher than for diffusion creep,
752 flow is expected to take place at very low stresses at high confining pressures of 2
753 GPa and higher.

754 The recrystallization mechanism of bulging recrystallization in quartz is usually
755 observed at low temperature conditions or the onset of crystal plastic deformation
756 (e.g., Stipp et al., 2002a, 2002b). The interaction of cracking and local grain
757 boundary migration indicates that some new grains in this recrystallization process
758 can be generated by cracking. One consequence of this process is that the host
759 control in new grain nucleation will be more difficult to determine, because small
760 rotation of new grains is likely, (e.g., van Daalen et al., 1999), but the rotation sense
761 and misorientation relationship is not necessarily clear and is not dependent on slip
762 systems.

763 Cracks are abundant in high pressure samples deformed by plastic mechanisms
764 at high temperature, in spite of the low deviatoric stress (~ 100 MPa) and the high
765 normal stress acting on any potential fracture plane ($P_C \sim 2$ GPa) – there is no or
766 very little displacement on these cracks. The interaction of cracking, crack healing,
767 and plasticity has been shown by Fitz Gerald et al. (1991) and Stünitz et al. (2017).
768 These observations suggest that in natural rocks, microcracks may play an important
769 role in the initiation of plastic deformation and during dynamic recrystallization, even
770 for the deep levels of the crust where high temperatures enable viscous deformation
771 at low deviatoric stresses.

772 **5. Conclusions**

773 The deformation of quartzites in the presence of 0.1 wt.% of added H₂O shows
774 decreasing flow stresses with increasing confining pressure. An r-value of 0.46 can
775 be fitted to the fugacity data, resulting in an m-value of ~ 1 for the fugacity coefficient
776 at an n-value of ~ 2 . In addition, the following observations have been made:

777 1. The dominant deformation process is crystal plasticity in original quartz grains,
778 so that the strain analysis of quartz grains matches the bulk sample strain with an

779 error of a few percent. Dynamic recrystallization and recovery processes are
780 observed, too, so that the dominant deformation mechanism is dislocation creep.
781 Some cracking occurs during plastic deformation, but as the cracks do not display
782 significant offset, their contribution to the bulk strain is negligible.

783 2. Dynamic recrystallization of the deforming quartz grains takes place by
784 progressive subgrain rotation and by local grain boundary migration. The grain
785 boundary migration affects small clasts produced by cracking as well as former
786 subgrains once high angle boundaries have been established. The recrystallized
787 material acquires a different luminescence colour (blue), which can be used to track
788 the recrystallized material in the microstructures. The processes indicate that
789 nucleation of new grains may take place by cracking (in addition to other processes)
790 and appears to be an important part of a process that is termed “bulging
791 recrystallization”.

792 3. The stress exponent n is approximately equal to 2, when some diffusive mass
793 transfer is important during dislocation creep. This contribution is likely to be fluid-
794 dependent or fluid enhanced.

795 4. The amount of recrystallized material increases with increasing confining
796 pressure. It is inferred that the increasing confining pressure has an enhancing effect
797 on the grain boundary migration rate and thus recrystallization rate.

798 **Acknowledgements**

799 We thank Rune Stien (ELKEM) and Raoul Heilbronner for their help with the
800 sampling of the quartzite at Austertana. We thank Ida Di Carlo for her support with
801 SEM-cathodoluminescence, Aneta Slodczyk for her precious help with FTIR
802 measurements, and Audrey Sauldubois for TEM support. We thank Greg Hirth and
803 Andreas Kronenberg for their very insightful and constructive reviews. P. Pongrac

804 acknowledges support from the grant agency of Charles University (GAUK 400/13)
805 and the Centre of Geosphere Dynamics (UNCE/SCI/006).

806 Support from the VOLTAIRE (ANR-10-LABX-100-01) and PLANEX (ANR-11-
807 EQPX-36) projects funded by ANR through the PIA (Programme d'Investissement
808 d'Avenir) is gratefully acknowledged.

809 **References**

- 810 Aasly, K., Malvik, T., Myrhaug, E.H., 2007. Advanced methods to characterize
811 thermal properties of quartz. Conf. Paper INFACON 11, Innovations in Ferro
812 Alloy Industry,
813 <http://citeseerx.ist.psu.edu/viewdoc/download?doi=10.1.1.607.1094&rep=rep1>
814 &type=pdf
- 815 Bachmann, F., Hielscher, R., Schaeben, H., 2011. Grain detection from 2d and 3d
816 EBSD data—Specification of the MTEX algorithm. *Ultramicroscopy* 111,
817 1720–1733. <https://doi.org/10.1016/j.ultramic.2011.08.002>
- 818 Bailey, J.E., Hirsch, P.B., 1962. The recrystallization process in some polycrystalline
819 metals. *Proc. Royal Soc. London, A* 267, 11-30.
- 820 Beeler, N.M., Hirth, G., Thomas, A., Bürgmann, R., 2016. Effective stress, friction,
821 and deep crustal faulting. *Journal of Geophysical Research: Solid Earth* 121,
822 1040–1059. <https://doi.org/10.1002/2015JB012115>
- 823 Bestmann, M., Pennacchioni, G., 2015. Ti distribution in quartz across a
824 heterogeneous shear zone within a granodiorite: The effect of deformation
825 mechanism and strain on Ti resetting. *Lithos* 227, 37–56.
826 <https://doi.org/10.1016/j.lithos.2015.03.009>
- 827 Blacic, J.D., 1981. Water diffusion in quartz at high pressure: Tectonic implications.
828 *Geophysical Research Letters* 8, 721–723.
829 <https://doi.org/10.1029/GL008i007p00721>

- 830 Dunge, H.B., 1962. Texture analysis in materials science—mathematical methods. Edn
831 Edn 2–35.
- 832 Chernak, L.J., Hirth, G., Selverstone, J., Tullis, J., 2009. Effect of aqueous and
833 carbonic fluids on the dislocation creep strength of quartz. *Journal of*
834 *Geophysical Research: Solid Earth* 114.
835 <https://doi.org/10.1029/2008JB005884>
- 836 Fitz Gerald, J.D., Boland, J.N., McLaren, A.C., Ord, A., Hobbs, B.E., 1991.
837 Microstructures in water-weakened single crystals of quartz. *Journal of*
838 *Geophysical Research* 96, 2139. <https://doi.org/10.1029/90JB02190>
- 839 Fukuda, J., Holyoke, C.W., Kronenberg, A.K., 2018. Deformation of Fine-Grained
840 Quartz Aggregates by Mixed Diffusion and Dislocation Creep. *Journal of*
841 *Geophysical Research: Solid Earth* 123, 4676–4696.
842 <https://doi.org/10.1029/2017JB015133>
- 843 Fusses, F., Regenauer-Lieb, K., Liu, J., Hough, R.M., De Carlo, F., 2009. Creep
844 cavitation can establish a dynamic granular fluid pump in ductile shear zones.
845 *Nature* 459, 974–977. <https://doi.org/10.1038/nature08051>
- 846 Gerretsen, J., Paterson, M.S., McLaren, A.C., 1989. The uptake and solubility of
847 water in quartz at elevated pressure and temperature. *Physics and Chemistry*
848 *of Minerals* 16. <https://doi.org/10.1007/BF00199553>
- 849 Gleason, G.C., Tullis, J., 1995. A flow law for dislocation creep of quartz aggregates
850 determined with the molten salt cell. *Tectonophysics* 247, 1-23
- 851 Götze, J., Plötze, M., Habermann, D., 2001. Origin, spectral characteristics and
852 practical applications of the cathodoluminescence (CL) of quartz - a review.
853 *Mineralogy and Petrology* 71, 225–250.
854 <https://doi.org/10.1007/s007100170040>
- 855 Griggs, D.T., Blacic, J.D., 1965. Quartz: Anomalous Weakness of Synthetic Crystals.
856 *Science* 147, 292–295. <https://doi.org/10.1126/science.147.3655.292>

- 857 Onyiah, D., 1997. Hydrolytic weakening of quartz and other silicates. *Geophysical*
858 *Journal of the Royal Astronomical Society* 14, 19–31.
859 <https://doi.org/10.1111/j.1365-246X.1967.tb06218.x>
- 860 Hamers, M.F., Pennock, G.M., Herwegh, M., Drury, M.R., 2016. Distinction between
861 amorphous and healed planar deformation features in shocked quartz using
862 composite color scanning electron microscope cathodoluminescence (SEM-
863 CL) imaging. *Meteoritics & Planetary Science* 51, 1914–1931.
864 <https://doi.org/10.1111/maps.12711>
- 865 Hamers, M.F., Pennock, G.M., Drury, M.R., 2017. Scanning electron microscope
866 cathodoluminescence imaging of subgrain boundaries, twins and planar
867 deformation features in quartz. *Physics and Chemistry of Minerals* 44, 263–
868 275.
- 869 Hansen, L.N., Zimmerman, M.E., Kohlstedt, D.L., 2012. The influence of
870 microstructure on deformation of olivine in the grain-boundary sliding regime.
871 *Journal of Geophysical Research: Solid Earth* 117.
872 <https://doi.org/10.1029/2012JB009305>
- 873 Heilbronner, R., 2002. Analysis of bulk fabrics and microstructure variations using
874 tessellations of autocorrelation functions. *Computers & Geosciences* 28, 447–
875 455. [https://doi.org/10.1016/S0098-3004\(01\)00088-7](https://doi.org/10.1016/S0098-3004(01)00088-7)
- 876 Heilbronner, R., Tullis, J., 2002. The effect of static annealing on microstructures and
877 crystallographic preferred orientations of quartzites experimentally deformed
878 in axial compression and shear. Geological Society, London, Special
879 Publications 200, 191–218. <https://doi.org/10.1144/GSL.SP.2001.200.01.12>
- 880 Heilbronner, R., Barrett, S., 2013. *Image Analysis in Earth Sciences: Microstructures*
881 *and Textures of Earth Materials*. Springer, 520 pp., Heidelberg.

- 882 Hirth, G., Tullis, J., 1992. Dislocation creep regimes in quartz aggregates. *Journal of*
883 *Structural Geology* 14, 145–159. [https://doi.org/10.1016/0191-](https://doi.org/10.1016/0191-8141(92)90053-Y)
884 [8141\(92\)90053-Y](https://doi.org/10.1016/0191-8141(92)90053-Y)
- 885 Hirth, G., Teyssier, C., Dunlap, J.W., 2001. An evaluation of quartzite flow laws
886 based on comparisons between experimentally and naturally deformed rocks.
887 *International Journal of Earth Sciences* 90, 77–87.
888 <https://doi.org/10.1007/s005310000152>
- 889 Hirth, G., Beeler, N.M., 2015. The role of fluid pressure on frictional behavior at the
890 base of the seismogenic zone. *Geology* 43, 223–226.
891 <https://doi.org/10.1130/G36361.1>
- 892 Holyoke, C.W., Kronenberg, A.K., 2010. Accurate differential stress measurement
893 using the molten salt cell and solid salt assemblies in the Griggs apparatus
894 with applications to strength, piezometers and rheology. *Tectonophysics* 494,
895 17–31. <https://doi.org/10.1016/j.tecto.2010.08.001>
- 896 Holyoke, C.W., Kronenberg, A.K., 2013. Reversible water weakening of quartz. *Earth*
897 *and Planetary Science Letters* 374, 185–190.
898 <https://doi.org/10.1016/j.epsl.2013.05.039>
- 899 Jaoul, O., Tullis, J., Kronenberg, A., 1984. The effect of varying water contents on
900 the creep behavior of Heavitree quartzite. *Journal of Geophysical Research:*
901 *Solid Earth* 89, 4298–4312. <https://doi.org/10.1029/JB089iB06p04298>
- 902 Kilian, R., Heilbronner, R., 2017. Analysis of crystallographic preferred orientations of
903 experimentally deformed Black Hills Quartzite. *Solid Earth* 8, 1095.
- 904 Kohlstedt, D.L., Evans, B., Mackwell, S.J., 1995. Strength of the lithosphere:
905 Constraints imposed by laboratory experiments. *Journal of Geophysical*
906 *Research: Solid Earth* 100, 17587–17602.
- 907 Kronenberg, A.K., Tullis, J., 1984. Flow strengths of quartz aggregates: Grain size
908 and pressure effects due to hydrolytic weakening. *Journal of Geophysical*

- 909 Research: Solid Earth 1201–1207.
910 [https://doi.org/10.1029/JB089iB06p04281@10.1002/\(ISSN\)2169-](https://doi.org/10.1029/JB089iB06p04281@10.1002/(ISSN)2169-)
911 9356.CHEMDEF1
- 912 Kronenberg, A.K., Kirby, S.H., Aines, R.D., Rossman, G.R., 1986. Solubility and
913 diffusional uptake of hydrogen in quartz at high water pressures: Implications
914 for hydrolytic weakening. *Journal of Geophysical Research: Solid Earth* 91,
915 12723–12741. <https://doi.org/10.1029/JB091iB12p12723>
- 916 Larrieu, T.L., Ayers, J.C., 1997. Measurements of the pressure-volume-temperature
917 properties of fluids to 20 kbar and 1000°C: A new approach demonstrated on
918 H₂O. *Geochimica et Cosmochimica Acta* 61, 3121–3134.
919 [https://doi.org/10.1016/S0016-7037\(97\)00155-5](https://doi.org/10.1016/S0016-7037(97)00155-5)
- 920 Lu, L.X., Jiang, D., 2019. Quartz Flow Law Revisited: The Significance of Pressure
921 Dependence of the Activation Enthalpy. *Journal of Geophysical Research:*
922 *Solid Earth* 124, 241–256. <https://doi.org/10.1029/2018JB016226>
- 923 Luan, F.C., Paterson, M.S., 1992. Preparation and deformation of synthetic
924 aggregates of quartz. *Journal of Geophysical Research: Solid Earth* 97, 301–
925 320. <https://doi.org/10.1029/91JB01748>
- 926 Mainprice, D.H., Paterson, M.S., 1984. Experimental studies of the role of water in
927 the plasticity of quartzites. *Journal of Geophysical Research: Solid Earth* 89,
928 4257–4269. <https://doi.org/10.1029/JB089iB06p04257>
- 929 Manning, C.E., 1994. The solubility of quartz in H₂O in the lower crust and upper
930 mantle. *Geochimica et Cosmochimica Acta* 58, 4831–4839.
931 [https://doi.org/10.1016/0016-7037\(94\)90214-3](https://doi.org/10.1016/0016-7037(94)90214-3)
- 932 Manning, C.E., 2018. Fluids of the deep crust: Deep is different. *Ann. Rev. Earth*
933 *Plan. Sci.* 46, 67-97. <https://doi.org/10.1146/annurev-earth-060614-105224>
- 934 McLaren, A.C., 2005. *Transmission Electron Microscopy of Minerals and Rocks.*
935 Cambridge University Press.

- 936 Menegon, L., Fusses, F., Stünitz, H., Xiao, X., 2019. Creep cavitation bands control
937 porosity and fluid flow in lower crustal shear zones. *Geology* 43, 227–230.
938 <https://doi.org/10.1130/G36307.1>
- 939 Negrini, M., Stünitz, H., Berger, A., Morales, L.F., 2014. The effect of deformation on
940 the TitaniQ geothermobarometer: an experimental study. *Contributions to*
941 *Mineralogy and Petrology* 167, 982.
- 942 Okazaki, K., Burdette, E., Hirth, G., 2021. Rheology of the Fluid Oversaturated Fault
943 Zones at the Brittle-Plastic Transition. *Journal of Geophysical Research: Solid*
944 *Earth* 126, e2020JB020804. <https://doi.org/10.1029/2020JB020804>
- 945 Okudaira, T., Jeřábek, P., Stünitz, H., Fusses, F., 2015. High-temperature fracturing
946 and subsequent grain-size-sensitive creep in lower crustal gabbros: Evidence
947 for coseismic loading followed by creep during decaying stress in the lower
948 crust? *Journal of Geophysical Research: Solid Earth* 120, 3119–3141.
949 <https://doi.org/10.1002/2014JB011708>
- 950 Palazzin, G., Raimbourg, H., Stünitz, H., Heilbronner, R., Neufeld, K., Précigout, J.,
951 2018. Evolution in H₂O contents during deformation of polycrystalline quartz:
952 An experimental study. *Journal of Structural Geology* 114, 95–110.
953 <https://doi.org/10.1016/j.jsg.2018.05.021>
- 954 Panozzo, R., 1984. Two-dimensional strain from the orientation of lines in a plane.
955 *Journal of Structural Geology, Planar and Linear Fabrics of Deformed Rocks*
956 6, 215–221. [https://doi.org/10.1016/0191-8141\(84\)90098-1](https://doi.org/10.1016/0191-8141(84)90098-1)
- 957 Paterson, M., Kekulawala, K.R.S.S., 1979. The role of water in quartz deformation [+
958 Discussions]. *Bulletin de Minéralogie* 102, 92–100.
959 <https://doi.org/10.3406/bulmi.1979.7261>
- 960 Paterson, M., 1982. The determination of hydroxyl by infrared absorption in quartz,
961 silicate glasses and similar materials. *Bulletin de Minéralogie* 105, 20–29.
962 <https://doi.org/10.3406/bulmi.1982.7582>

- 963 Paterson, M.S., Luan, F.C., 1990. Quartzite rheology under geological conditions.
964 Geological Society, London, Special Publications 54, 299–307.
965 <https://doi.org/10.1144/GSL.SP.1990.054.01.26>
- 966 Paterson, M.S., Wong, T. (Eds.), 2005. Evolution of Physical Properties during Brittle
967 Failure. Experimental Rock Deformation — The Brittle Field. Springer, Berlin,
968 Heidelberg, 59–114. https://doi.org/10.1007/3-540-26339-X_5
- 969 Paterson, M.S., 2012. Materials Science for Structural Geology. Springer Science &
970 Business Media.
- 971 Pec, M., Stünitz, H., Heilbronner, R., Drury, M., 2016. Semi-brittle flow of granitoid
972 fault rocks in experiments. *Journal of Geophysical Research: Solid Earth* 121,
973 1677–1705. <https://doi.org/10.1002/2015JB012513>
- 974 Pevik, J.A., 2015. Geological and Mineralogical Characterization of the Upper Part of
975 the Gamasfjell Quartzite at the Vaggecearu Mountain. MSc thesis, 132 pp.,
976 NTNU Trondheim
- 977 Pitzer, K.S., Sterner, S.M., 1994. Equations of state valid continuously from zero to
978 extreme pressures for H₂O and CO₂. *The Journal of Chemical Physics* 101,
979 3111–3116.
- 980 Post, A.D., Tullis, J., Yund, R.A., 1996. Effects of chemical environment on
981 dislocation creep of quartzite. *Journal of Geophysical Research: Solid Earth*
982 101, 22143–22155. <https://doi.org/10.1029/96JB01926>
- 983 Précigout, J., Stünitz, H., 2016. Evidence of phase nucleation during olivine diffusion
984 creep: A new perspective for mantle strain localisation. *Earth and Planetary*
985 *Science Letters* 455, 94–105. <https://doi.org/10.1016/j.epsl.2016.09.029>
- 986 Précigout, J., Prigent, C., Palasse, L., Pochon, A., 2017. Water pumping in mantle
987 shear zones. *Nature Communications* 8, 15736.
988 <https://doi.org/10.1038/ncomms15736>

- 989 Précigout, J., Stünitz, H., Pinquier, F., Champain, R., Goubaert, A., 2018. High-
990 pressure, High-temperature Deformation Experiment Using the New
991 Generation Griggs-type Apparatus. *JoVE (Journal of Visualized Experiments)*
992 e56841. <https://doi.org/10.3791/56841>
- 993 Précigout, J., Stünitz, H., Villeneuve, J., 2019. Excess water storage induced by
994 viscous strain localization during high-pressure shear experiment. *Scientific*
995 *Reports* 9, 3463. <https://doi.org/10.1038/s41598-019-40020-y>
- 996 Ramseyer, K., Baumann, J., Matter, A., Mullis, J., 1988. Cathodoluminescence
997 Colours of α -Quartz. *Mineralogical Magazine* 52, 669–677.
998 <https://doi.org/10.1180/minmag.1988.052.368.11>
- 999 Richter, B., Stünitz, H., Heilbronner, R., 2018. The brittle-to-viscous transition in
1000 polycrystalline quartz: An experimental study. *Journal of Structural Geology*
1001 114, 1–21. <https://doi.org/10.1016/j.jsg.2018.06.005>
- 1002 Rutter, E.H., Brodie, K.H., 2004a. Experimental intracrystalline plastic flow in hot-
1003 pressed synthetic quartzite prepared from Brazilian quartz crystals. *Journal of*
1004 *Structural Geology* 26, 259–270. <https://doi.org/10.1016/S0191->
1005 [8141\(03\)00096-8](https://doi.org/10.1016/S0191-8141(03)00096-8)
- 1006 Rutter, E. H., Brodie, K.H., 2004b. Experimental grain size-sensitive flow of hot-
1007 pressed Brazilian quartz aggregates. *Journal of Structural Geology* 26, 2011–
1008 2023. <https://doi.org/10.1016/j.jsg.2004.04.006>
- 1009 Skemer, P., Katayama, I., Jiang, Z., Karato, S., 2005. The misorientation index:
1010 Development of a new method for calculating the strength of lattice-preferred
1011 orientation. *Tectonophysics* 411, 157–167.
1012 <https://doi.org/10.1016/j.tecto.2005.08.023>
- 1013 Spear, F.S., Wark, D.A., 2009. Cathodoluminescence imaging and titanium
1014 thermometry in metamorphic quartz. *Journal of Metamorphic Geology* 27,
1015 187–205. <https://doi.org/10.1111/j.1525-1314.2009.00813.x>

- 1016 Stipp, M., Stünitz, H., Heilbronner, R., Schmid, S.M., 2002a. The eastern Tonale fault
1017 zone: a 'natural laboratory' for crystal plastic deformation of quartz over a
1018 temperature range from 250 to 700°C. *Journal of Structural Geology* 24,
1019 1861–1884. [https://doi.org/10.1016/S0191-8141\(02\)00035-4](https://doi.org/10.1016/S0191-8141(02)00035-4)
- 1020 Stipp, M., Stünitz, H., Heilbronner, R., Schmid, S.M., 2002b. Dynamic
1021 recrystallization of quartz: correlation between natural and experimental
1022 conditions. *Geological Society, London, Special Publications* 200, 171–190.
1023 <https://doi.org/10.1144/GSL.SP.2001.200.01.11>
- 1024 Stipp, M., Kunze, K., 2008. Dynamic recrystallization near the brittle-plastic transition
1025 in naturally and experimentally deformed quartz aggregates. *Tectonophysics*
1026 448, 77–97. <https://doi.org/10.1016/j.tecto.2007.11.041>
- 1027 Stöckhert, B., Massonne, H.-J., Ursula Nowlan, E., 1997. Low differential stress
1028 during high-pressure metamorphism: The microstructural record of a
1029 metapelite from the Eclogite Zone, Tauern Window, Eastern Alps. *Lithos* 41,
1030 103–118. [https://doi.org/10.1016/S0024-4937\(97\)82007-5](https://doi.org/10.1016/S0024-4937(97)82007-5)
- 1031 Stöckhert, B., Renner, J., 1998. Rheology of Crustal Rocks at Ultrahigh Pressure. In:
1032 Hacker, B.R., Liou, J.G. (Eds.), *When Continents Collide: Geodynamics and*
1033 *Geochemistry of Ultrahigh-Pressure Rocks, Petrology and Structural Geology.*
1034 Springer Netherlands, Dordrecht, 57–95. [https://doi.org/10.1007/978-94-015-](https://doi.org/10.1007/978-94-015-9050-1_3)
1035 [9050-1_3](https://doi.org/10.1007/978-94-015-9050-1_3)
- 1036 Stöckhert, B., Wachmann, M., Küster, M., Bimmermann, S., 1999. Low effective
1037 viscosity during high pressure metamorphism due to dissolution precipitation
1038 creep: the record of HP–LT metamorphic carbonates and siliciclastic rocks
1039 from Crete. *Tectonophysics* 303, 299–319. [https://doi.org/10.1016/S0040-](https://doi.org/10.1016/S0040-1951(98)00262-5)
1040 [1951\(98\)00262-5](https://doi.org/10.1016/S0040-1951(98)00262-5)

- 1041 Stockert, B., 2002. Stress and deformation in subduction zones: insight from the
1042 record of exhumed metamorphic rocks. Geological Society, London, Special
1043 Publications 200, 255–274.
- 1044 Stünitz, H., Fitz Gerald, J.D., Tullis, J., 2003. Dislocation generation, slip systems,
1045 and dynamic recrystallization in experimentally deformed plagioclase single
1046 crystals. Tectonophysics 372, 215–233. [https://doi.org/10.1016/S0040-](https://doi.org/10.1016/S0040-1951(03)00241-5)
1047 [1951\(03\)00241-5](https://doi.org/10.1016/S0040-1951(03)00241-5)
- 1048 Stünitz, H., Thust, A., Heilbronner, R., Behrens, H., Kilian, R., Tarantola, A., Gerald,
1049 J.D.F., 2017. Water redistribution in experimentally deformed natural milky
1050 quartz single crystals—Implications for H₂O-weakening processes. Journal of
1051 Geophysical Research: Solid Earth 122, 866–894.
1052 <https://doi.org/10.1002/2016JB013533>
- 1053 Tarantola, A., Diamond, L.W., Stünitz, H., 2010. Modification of fluid inclusions in
1054 quartz by deviatoric stress I: experimentally induced changes in inclusion
1055 shapes and microstructures. Contributions to Mineralogy and Petrology 160,
1056 825–843. <https://doi.org/10.1007/s00410-010-0509-z>
- 1057 Tarantola, A., Diamond, L.W., Stünitz, H., 2010. Modification of fluid inclusions in
1058 quartz by deviatoric stress I: experimentally induced changes in inclusion
1059 shapes and microstructures. Contributions to Mineralogy and Petrology 160,
1060 825–843. <https://doi.org/10.1007/s00410-010-0509-z>
- 1061 Tokle, L., Hirth, G., Behr, W.M., 2019. Flow laws and fabric transitions in wet
1062 quartzite. Earth and Planetary Science Letters 505, 152–161.
1063 <https://doi.org/10.1016/j.epsl.2018.10.017>
- 1064 Trépiéd, L., Doukhan, J.C., Paquet, J., 1980. Subgrain boundaries in quartz
1065 theoretical analysis and microscopic observations. Physics and Chemistry of
1066 Minerals 5, 201–218.

- 1067 Tullis, J., Chen, C.E., Yund, R.A., 1979. Pressure dependence of rock strength.
1068 implications for hydrolytic weakening. *Bulletin de Minéralogie* 102, 110–114.
1069 <https://doi.org/10.3406/bulmi.1979.7263>
- 1070 Tullis, J., Yund, R.A., 1989. Hydrolytic weakening of quartz aggregates: The effects
1071 of water and pressure on recovery. *Geophysical Research Letters* 16, 1343–
1072 1346. <https://doi.org/10.1029/GL016i011p01343>
- 1073 van Daalen, M., Heilbronner, R., Kunze, K., 1999. Orientation analysis of localized
1074 shear deformation in quartz fibres at the brittle–ductile transition.
1075 *Tectonophysics* 303, 83–107. [https://doi.org/10.1016/S0040-1951\(98\)00264-9](https://doi.org/10.1016/S0040-1951(98)00264-9)
- 1076 Vernooij, M.G.C., den Brok, B., Kunze, K., 2006. Development of crystallographic
1077 preferred orientations by nucleation and growth of new grains in
1078 experimentally deformed quartz single crystals. *Tectonophysics, Deformation
1079 Mechanisms, Microstructure and Rheology of Rocks in Nature and
1080 Experiment* 427, 35–53. <https://doi.org/10.1016/j.tecto.2006.06.008>
- 1081 Wassmann, S., Stöckhert, B., 2013. Low stress deformation of garnet by incongruent
1082 dissolution precipitation creep. *Journal of Structural Geology* 46, 200–219.
1083 <https://doi.org/10.1016/j.jsg.2012.09.002>

1084 **Figures and Tables**

1085 Figure 1. (a) Cross-polarized microphotograph of starting material Tana quartzite
1086 showing equant grains without undulatory extinction. (b) Pole figure of random
1087 crystallographic orientation of c-axis from 500 grains measured by EBSD. (c & d)
1088 Plane polarized light microscope-cathodoluminescence images: equant and rounded
1089 sand grains of various tints are surrounded by darker cement that grows in
1090 crystallographic continuity (arrows).

1091 Figure 2. Mechanical data for samples deformed in wet conditions (0.1 wt.% H₂O
1092 added) at 900°C for confining pressures between 600 and 2000 MPa. Samples ...LN

1093 have been deformed in Tromsø (Norway) whereas samples OR... have been
1094 deformed in Orléans (France). The samples strengths systematically decrease with
1095 increasing confining pressure.

1096 Figure 3. (a) Stress strain curves obtained for strain rate stepping experiments at 800
1097 MPa (OR79) and 2000 MPa (OR68). (b) Plot of the log strain rate vs. log flow stress.
1098 Solid circles are data obtained from strain rate stepping experiments whereas open
1099 circles are data from samples deformed at 10^{-6} s^{-1} constant strain rate at the same
1100 confining pressures. The slopes of the regressed lines indicate n-values of ~ 1.40 at
1101 2000 MPa and ~ 1.42 at 800 MPa.

1102 Figure 4. Cross polarized light images of sample OR32 deformed at 1000 MPa
1103 confining pressure. Left: overview of sample showing higher strain regions near the
1104 centre of the sample. In the most strongly deformed part of the sample, clasts are
1105 elongated, and limited recrystallization is observed at grain boundaries (core-mantle
1106 structures). Right: details of the recrystallized region showing undulatory extinction,
1107 subgrains, and new grains. The shortening direction is vertical.

1108 Figure 5. SEM-cathodoluminescence images of (a) starting material and of samples
1109 deformed at confining pressure of (b) 700 MPa (OR52), (c) 1000 MPa (546LN), (d)
1110 1500 MPa (OR64), (e) 2000 MPa (OR62) and (f) 2000 MPa high-strain (74%; OR56).
1111 The shortening direction is vertical for images (b-f).

1112 Figure 6. (a & b) SEM-CL-images of cracks in both cement and grains in sample
1113 deformed at (a) 800 (OR42) and (b) 1000 MPa (546LN) confining pressure. (c)
1114 Crystal faces at open grain boundary region in 546LN sample (1000 MPa). (d)
1115 Crystal faces in small luminescent grains in open space between grains in OR64
1116 sample (1500 MPa). The shortening direction is vertical for all images.

1117 Figure 7. Left: mosaic of OR57 sample (2000 MPa) in polarized light with associated
1118 SEM-CL-images longitudinal transect. Right: examples of segmentation and
1119 identification of bright luminescent zones (coloured in blue).

1120 Figure 8. Percentage of bright luminescence for SEM-CL images longitudinal
1121 transects, (a) as a function of the position along the sample and (b) as a function of
1122 the confining pressure.

1123 Figure 9. Example of the manual segmentation made for the OR62 (2000 MPa) thin
1124 section from optical cathodoluminescence images. Interiors of grains are isolated
1125 from the surrounding cement based on their luminescence colour contrasts. The
1126 shortening direction is vertical.

1127 Figure 10. SURFOR projections curves showing that the starting material TQ2 has a
1128 slight strain of 3.5% whereas deformed samples at various confining pressures have
1129 an orientation comprise between 80 and 90° for a strain comprise between 24.6%
1130 (546LN) and 34.4% (OR52). The global shortening direction for deformed samples is
1131 theoretically 90°.

1132 Figure 11. Cathodoluminescence (CL) image, EBSD orientation map and inverse
1133 pole figures (IPF) for sample 546LN. (a) CL image with blue (380-515 nm) optical
1134 filter to highlight recrystallized areas; (b) EBSD map of quartz orientations coloured
1135 parallel to the X direction, sample is plotted with hexagonal symmetry (6/mmm) to
1136 account for the effect of Dauphiné twins. Grain boundaries are identified by black
1137 bounding lines and subgrains are identified by white boundaries. (c) IPF's for
1138 subgrain (defined by a misorientation between 2 and 10°) boundaries and (d) grain
1139 (defined by a misorientation greater than 10°) boundaries. All IPF's are plotted in
1140 hexagonal 6/mmm symmetry with the same scale for multiples of uniform (m.u.d.) for
1141 each plot. (e) Colour key for IPF || X map.

1142 Figure 12. Cathodoluminescence (CL) image, EBSD orientation map, misorientation
1143 map and inverse pole figures (IPF) for high strain sample OR56. (a) CL image with
1144 blue (380-515 nm) filter to highlight recrystallized areas. (b) EBSD map of quartz
1145 orientations coloured parallel to the X direction, sample is plotted with hexagonal
1146 symmetry (6/mmm) to account for the effects of Dauphiné twins. Grain boundaries
1147 are identified by black bounding lines and subgrains are identified by white
1148 boundaries (see detailed insert at the top right hand corner). (c) Misorientation map
1149 where blue shows low misorientation and yellow shows high misorientation relative
1150 to the mean grain orientation. Grains 1744 and 3542 are highlighted on the IPF (bold
1151 black) and misorientation (red) maps. (d-f) IPF's for subgrain (defined by a
1152 misorientation between 2 and 10°) and grain (defined by a misorientation greater
1153 than 10°) boundaries with the d) full map, (e) grain 1744 and (f) grain 3542. All IPF's
1154 are plotted in hexagonal 6/mmm symmetry with the same scale for multiples of
1155 uniform distribution (m.u.d.) for each plot.

1156 Figure 13. Log₁₀ grain size distributions for samples (a) 546LN and (b) OR56. Grain
1157 size distributions are separated into relict, recrystallized and subgrain populations.

1158 Figure 14. A power-law relationship fitted to the flow stresses (at 15% strain) at
1159 different confining pressures.

1160 Figure 15. Relationship between water fugacity and flow stresses. The slope
1161 indicates a m/n coefficient of 0.46 for the values obtained in this study for Tana
1162 quartzite. Results from published studies are included for comparison.

1163 Figure 16. Sketch of the grain assemblage evolution during deformation.

1164 Table 1. Grain parameters for starting material Tana quartzite calculated from
1165 segmentation of both cross-polarized (CP) and cathodoluminescence (CL) light
1166 microscopy images. D_{eq} is the equivalent diameter (diameter of a circle of the same

1167 area than the grain) and AR is the Aspect Ratio (ratio of major and minor axes of the
1168 ellipse fitting).

1169 Table 2. Experimental conditions of deformed samples.

1170 Table 3. Flow stresses obtained and corresponding strain rates for the two strain rate
1171 stepping experiments performed.

1172 Table 4. Results from particle analysis. The errors correspond to the standard
1173 deviation.

1174 Table 5. Results from SURFOR analysis. For the finite sample strain, the first column
1175 corresponds to the calculated strain and the second column to the measured strain
1176 (refer to Table 2. for details).

1177 Table 6. Grain sizes obtained from EBSD analysis on 546LN (1000 MPa) and OR56
1178 (2000 MPa, high-strained) samples (corresponding maps in Figs.11 & 12).

Table 1. Grain parameters for starting material Tana quartzite calculated from segmentation of both cross-polarized (CP) and cathodoluminescence (CL) light microscopy images. D_{eq} is the equivalent diameter (diameter of a circle of the same area than the grain) and AR is the Aspect Ratio (ratio of major and minor axes of the ellipse fitting).

	d_{eq} (μm)	AR	d_{eq} (μm)	AR
	CP-image analysis		LM-CL-image analysis	
N	1423		2103	
Mean	203.71	1.56	186.18	1.55
Median	198.20	1.47	178.60	1.46
RMS	210.78	-	196.14	-
SD	54.16	0.38	61.72	0.38
Max	451.49	3.54	476.29	4.68
Min	210.78	1.01	57.47	1.01

Table 2. Experimental conditions of deformed samples.

Sample name	Griggs apparatus	Temperature (°C)	Water added (wt.%)	Confining pressure (MPa)	Strain rate (s ⁻¹)	Shortening calculated (%)	Shortening measured (%)
542LN	Tromsø	900	0.1	600	1.29E-06	33.46	30.48
544LN				1500	1.37E-06	33.48	30.71
546LN				1000	1.28E-06	31.27	28.01
OR32				1000	9.32E-07	30.96	29.39
OR42				800	8.12E-07	29.71	30.83
OR48				1250	8.80E-07	28.42	27.71
OR52				700	8.26E-07	31.98	32.12
OR56	Orléans	900	0.1	2000	<i>not determined</i>		74.43
OR57				2000	<i>not determined</i>		27.76
OR60				600	7.33E-07	30.92	30.57
OR62				2000	9.29E-07	30.53	29.51
OR64				1500	9.40E-07	29.76	26.59
OR59				1000	Hot pressed (251.7h)		0.53
OR66				2000	Hot pressed (216.8h)		-
OR68	2000	Strain rate stepping					
OR79	800	Strain rate stepping					

*error is estimated to be up to 0.8% for a measuring error of 0.1 mm

Table 3. Flow stresses obtained and corresponding strain rates for the two strain rate stepping experiments performed.

Sample	OR68	OR79
Pressure (MPa)	2000	800
Temperature (°C)	900	
Diff. stress at 10^{-5} s^{-1}	200.6	471.7
Diff. stress at 10^{-6} s^{-1}	85.4	164.3
Diff. stress at 10^{-7} s^{-1}	10.0	65.3
Diff. stress at 10^{-5} s^{-1}	265.2	633.4

Table 4. Results from particle analysis. The errors correspond to the standard deviation.

Sample	Confining pressure (MPa)	Number of grains analysed	Equivalent diameter (μm)	Aspect Ratio
TQ2	Starting material	2103	186 ± 62	1.55 ± 0.38
OR52	700	2203	174 ± 62	1.95 ± 0.64
546LN	1000	1116	230 ± 69	1.76 ± 0.54
OR32	1000	1835	204 ± 69	2.05 ± 0.73
OR64	1500	2603	172 ± 54	1.81 ± 0.55
OR62	2000	3072	181 ± 66	1.85 ± 0.57

Table 5. Results from SURFOR analysis. For the finite sample strain, the first column corresponds to the calculated strain and the second column to the measured strain (refer to Table 2. for details).

Sample	Confining pressure (MPa)	Minimum of the projection curve	Angle of minimum (°)	Angle(s) of maximum (°)	Fabric anisotropy (%)	Finite sample strains (%)	
						Calc.	Meas.
TQ2	Starting material	0.965	70	160 – 165	3.5	-	-
OR52	700	0.656	90	0 – 175	34.4	31.98	32.12
546LN	1000	0.754	85	170 – 175	24.60	31.27	28.01
OR32	1000	0.628	90	0 – 180	37.2	30.96	29.39
OR64	1500	0.722	80	170	27.8	29.76	26.59
OR62	2000	0.718	85	170 – 175	28.2	30.53	29.51

Table 6. Grain sizes obtained from EBSD analysis on 546LN (1000 MPa) and OR56 (2000 MPa, high-strained) samples (corresponding maps in Figs.11 & 12).

	546LN			OR56		
	Relict grains	Recryst. grains	Subgrains	Relict grains	Recryst. grains	Subgrains
Arith. Mean	7.967	3.789	3.854	9.030	3.323	2.683
Geom. Mean	7.595	3.291	2.884	8.314	2.825	2.121
RMS	8.613	4.282	4.879	9.853	3.824	3.871
Median	7.930	3.450	3.230	8.091	2.968	2.252
Mode	7 – 8	3.5 – 4 4.5 – 5	4 – 4.5	7 – 9	3.2 – 3.6	1.5 – 1.7
Std. Dev.	2.603	2.003	2.993	3.955	1.894	2.790

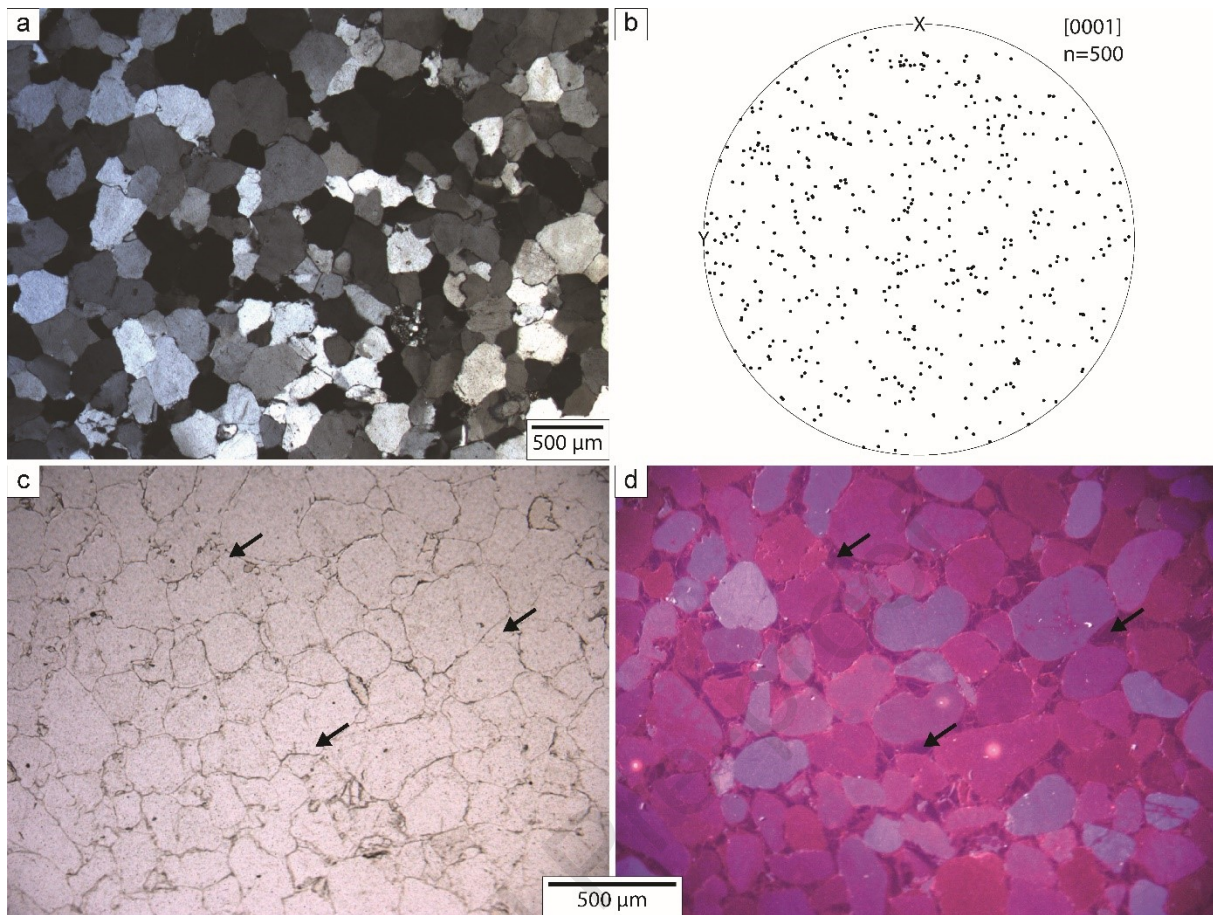


Figure 1. (a) Cross-polarized microphotograph of starting material Tana quartzite showing equant grains without undulatory extinction. (b) Pole figure of random crystallographic orientation of c-axis from 500 grains measured by EBSD. (c & d) Plane polarized light microscope-cathodoluminescence images: equant and rounded sand grains of various tints are surrounded by darker cement that grows in crystallographic continuity (arrows).

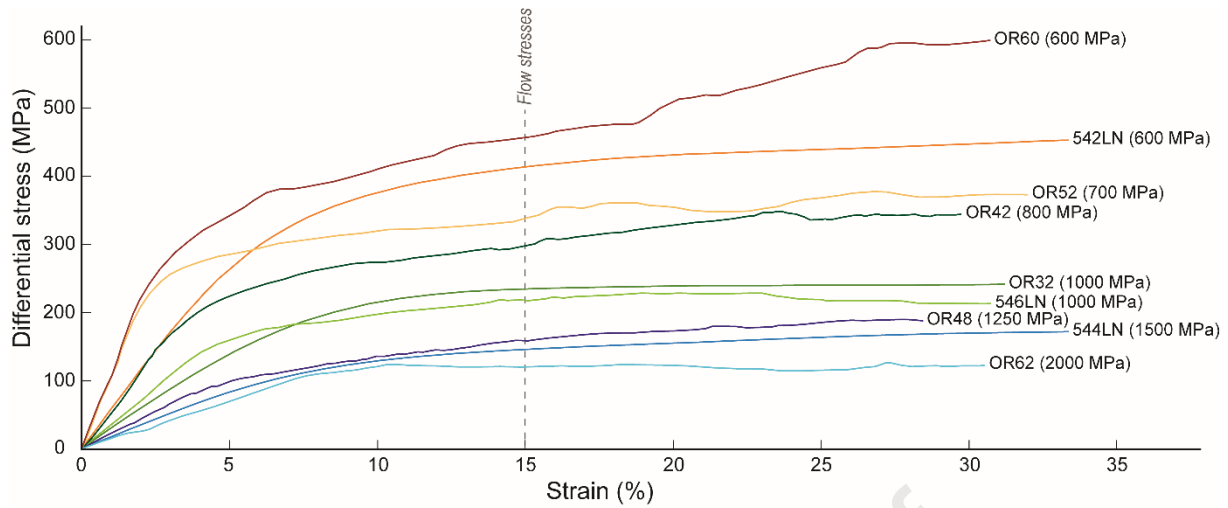


Figure 2. Mechanical data for samples deformed in wet conditions (0.1 wt.% H₂O added) at 900°C for confining pressures between 600 and 2000 MPa. Samples ...LN have been deformed in Tromsø (Norway) whereas samples OR... have been deformed in Orléans (France). The samples strengths systematically decrease with increasing confining pressure.

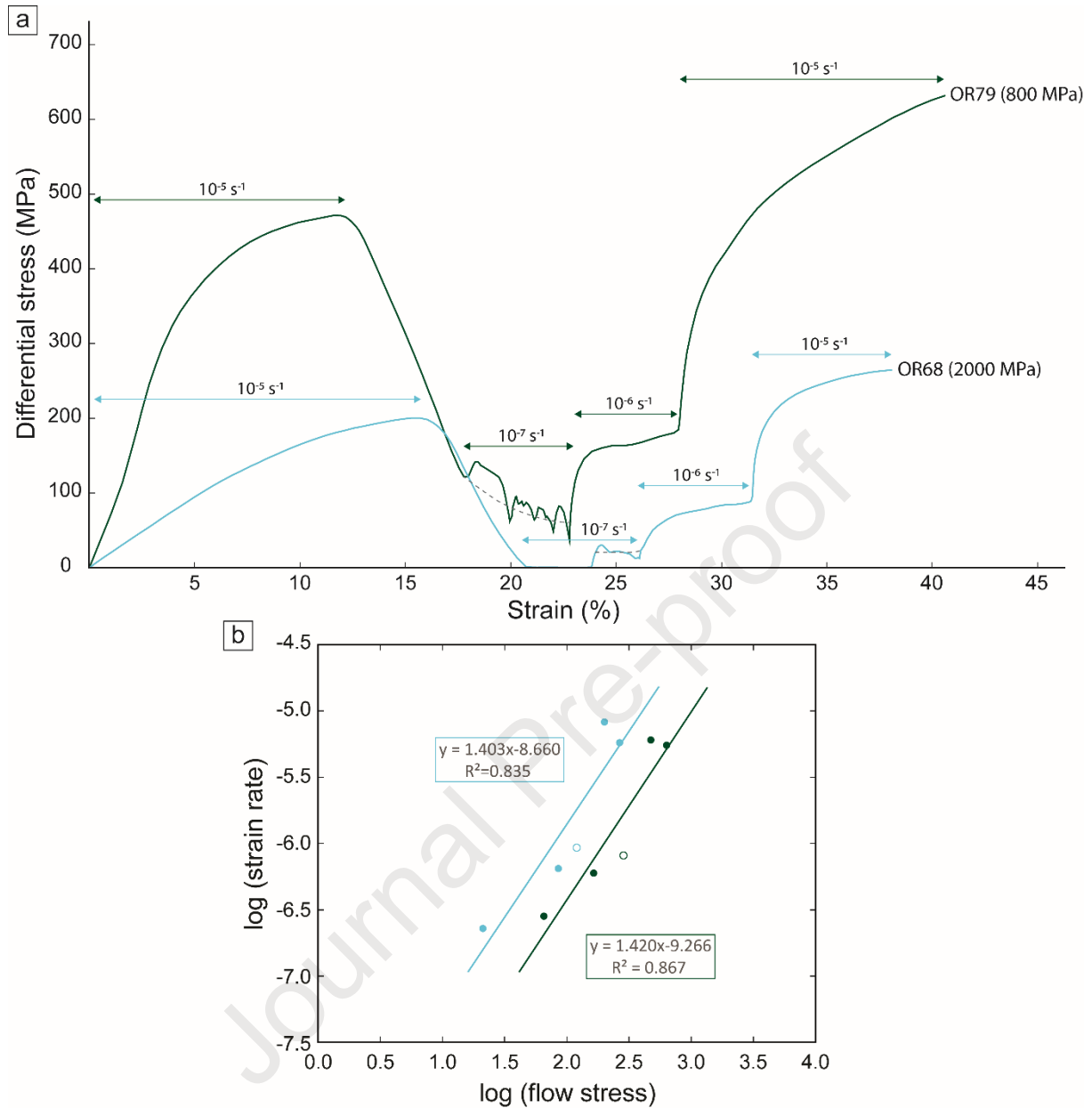


Figure 3. (a) Stress strain curves obtained for strain rate stepping experiments at 800 MPa (OR79) and 2000 MPa (OR68). (b) Plot of the log strain rate vs. log flow stress. Solid circles are data obtained from strain rate stepping experiments whereas open circles are data from samples deformed at 10^{-6} s^{-1} constant strain rate at the same confining pressures. The slopes of the regressed lines indicate n -values of ~ 1.89 at 2000 MPa and ~ 2.06 at 800 MPa.

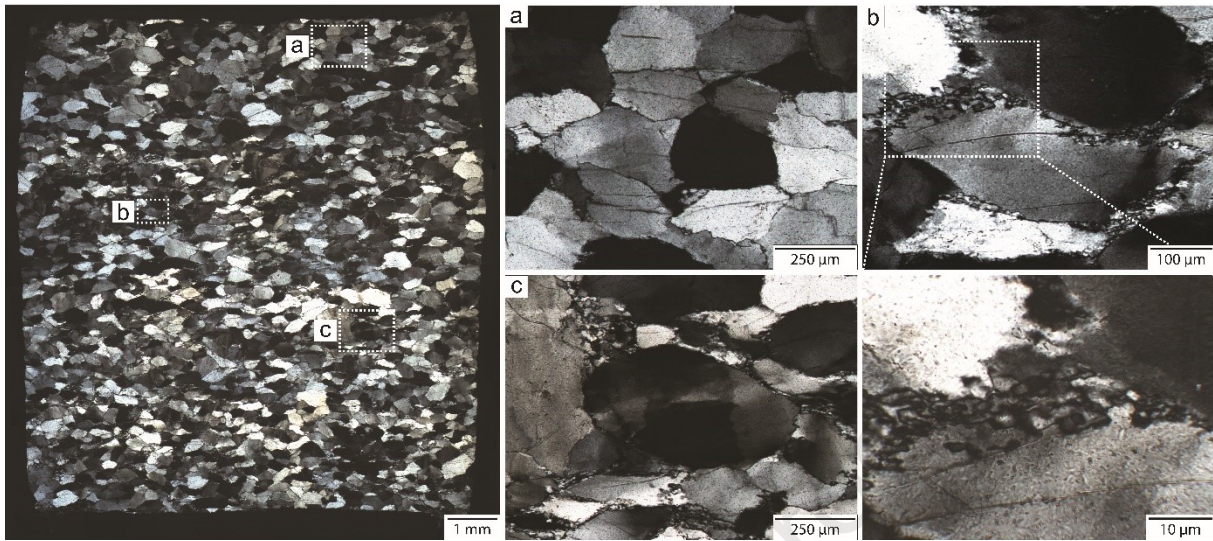


Figure 4. Cross polarized light images of sample OR32 deformed at 1000 MPa confining pressure. Left: overview of sample showing higher strain regions near the centre of the sample. In the most strongly deformed part of the sample, clasts are elongated, and limited recrystallization is observed at grain boundaries (core-mantle structures). Right: details of the recrystallized region showing undulatory extinction, subgrains, and new grains. The shortening direction is vertical.

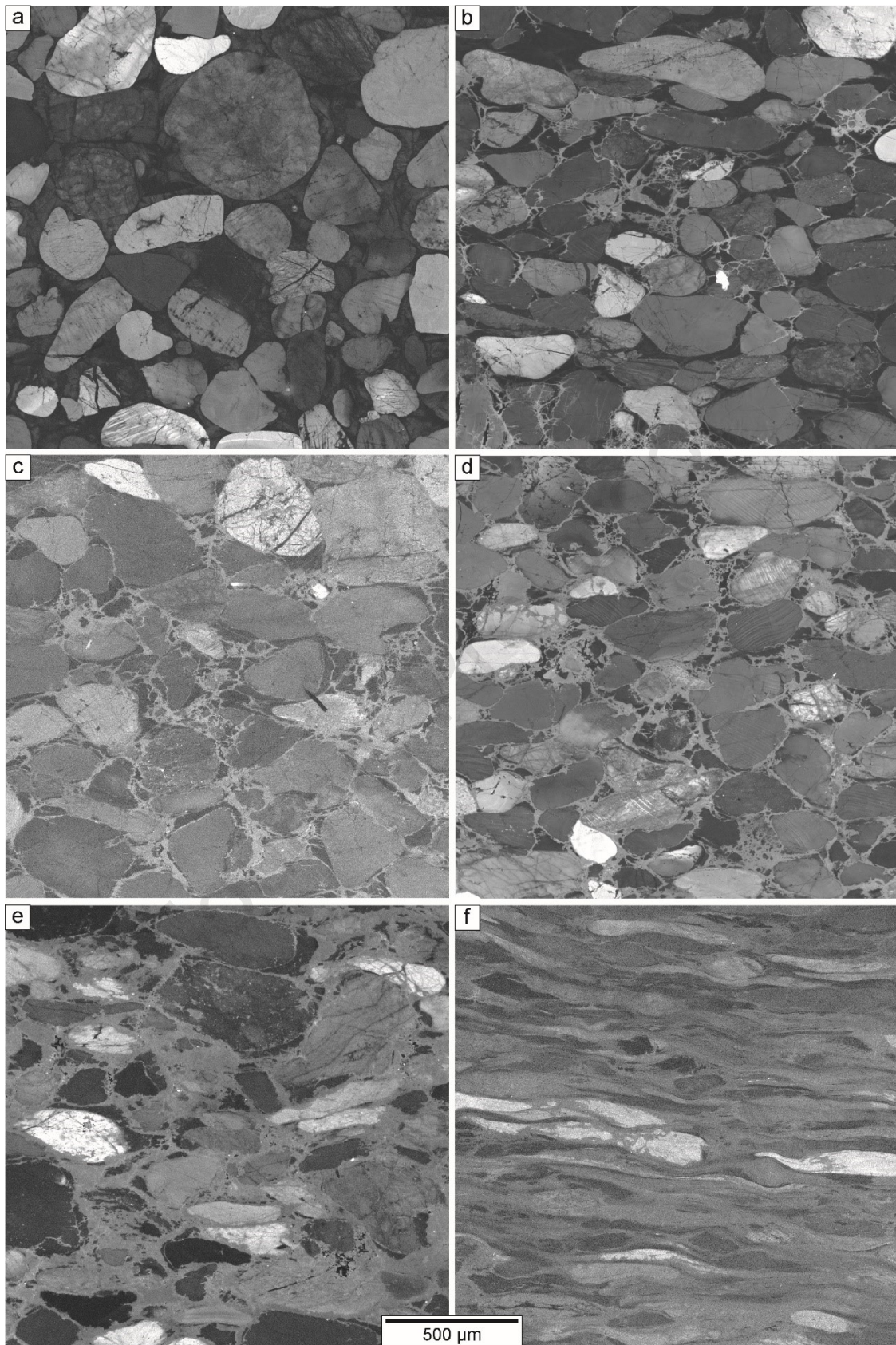


Figure 5. SEM-cathodoluminescence images of (a) starting material and of samples deformed at confining pressure of (b) 700 MPa (OR52), (c) 1000 MPa (546LN), (d) 1500 MPa (OR64), (e) 2000 MPa (OR62) and (f) 2000 MPa high-strain (74%; OR56). The shortening direction is vertical for images (b-f).

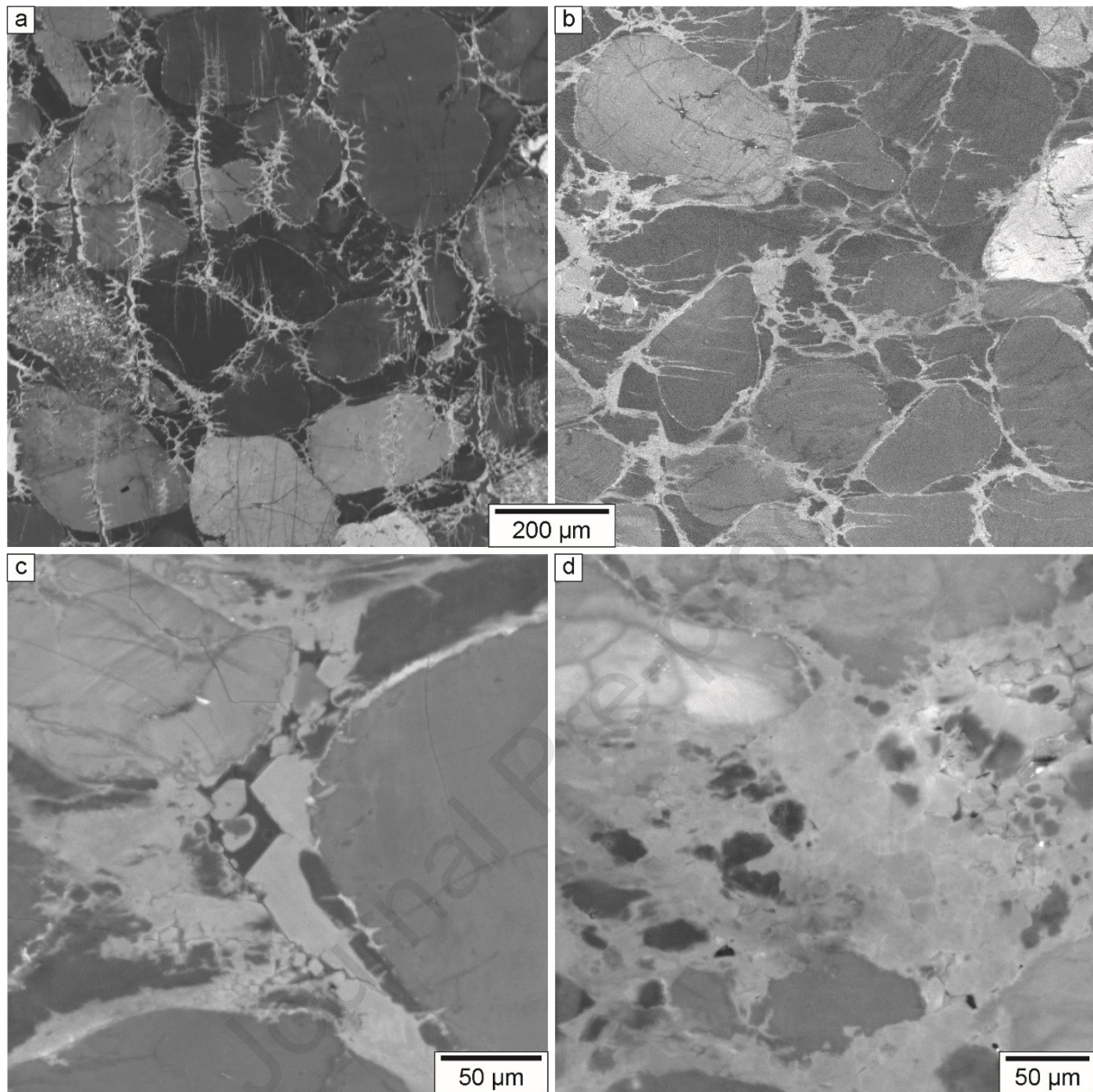


Figure 6. (a & b) SEM-CL-images of cracks in both cement and grains in sample deformed at (a) 800 (OR42) and (b) 1000 MPa (546LN) confining pressure. (c) Crystal faces at open grain boundary region in 546LN sample (1000 MPa). (d) Crystal faces in small luminescent grains in open space between grains in OR64 sample (1500 MPa). The shortening direction is vertical for all images.

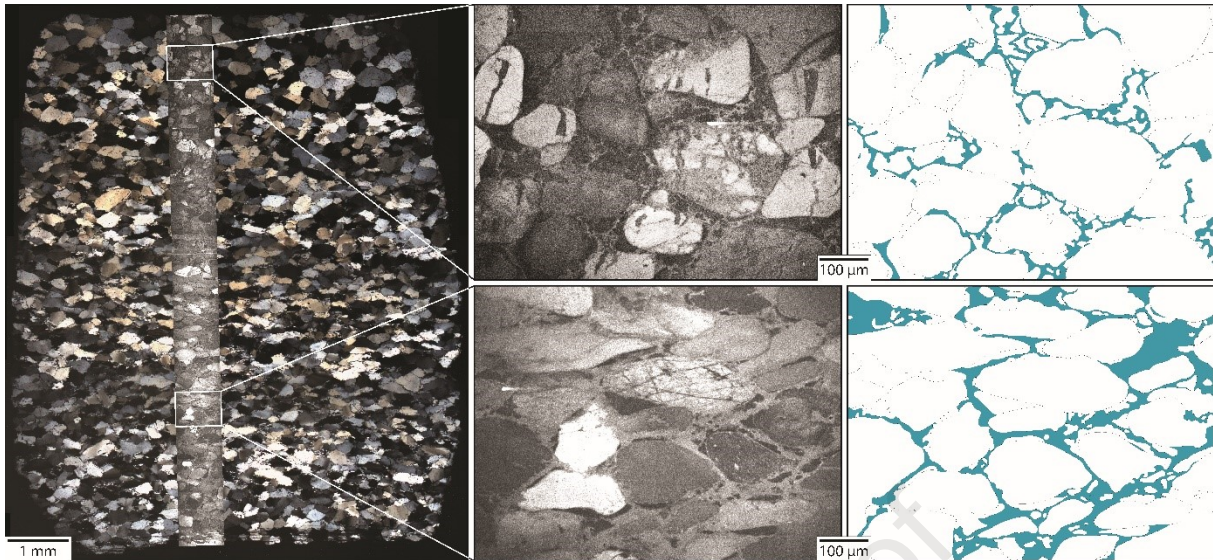


Figure 7. Left: mosaic of OR57 sample (2000 MPa) in polarized light with associated SEM-CL-images longitudinal transect. Right: examples of segmentation and identification of bright luminescent zones (coloured in blue).

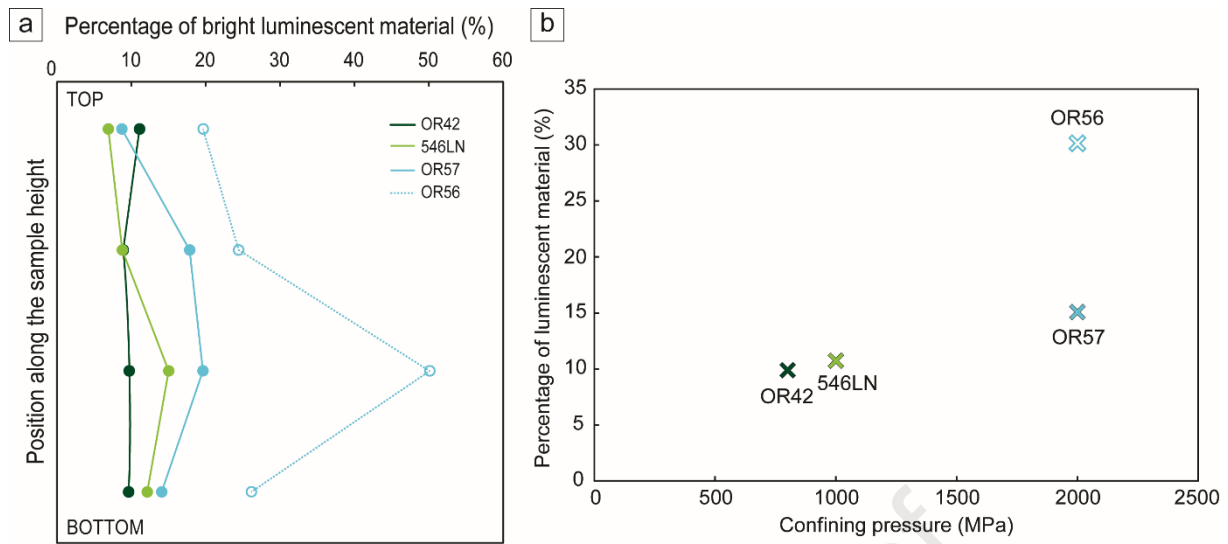


Figure 8. Percentage of bright luminescence for SEM-CL images longitudinal transects, (a) as a function of the position along the sample and (b) as a function of the confining pressure.

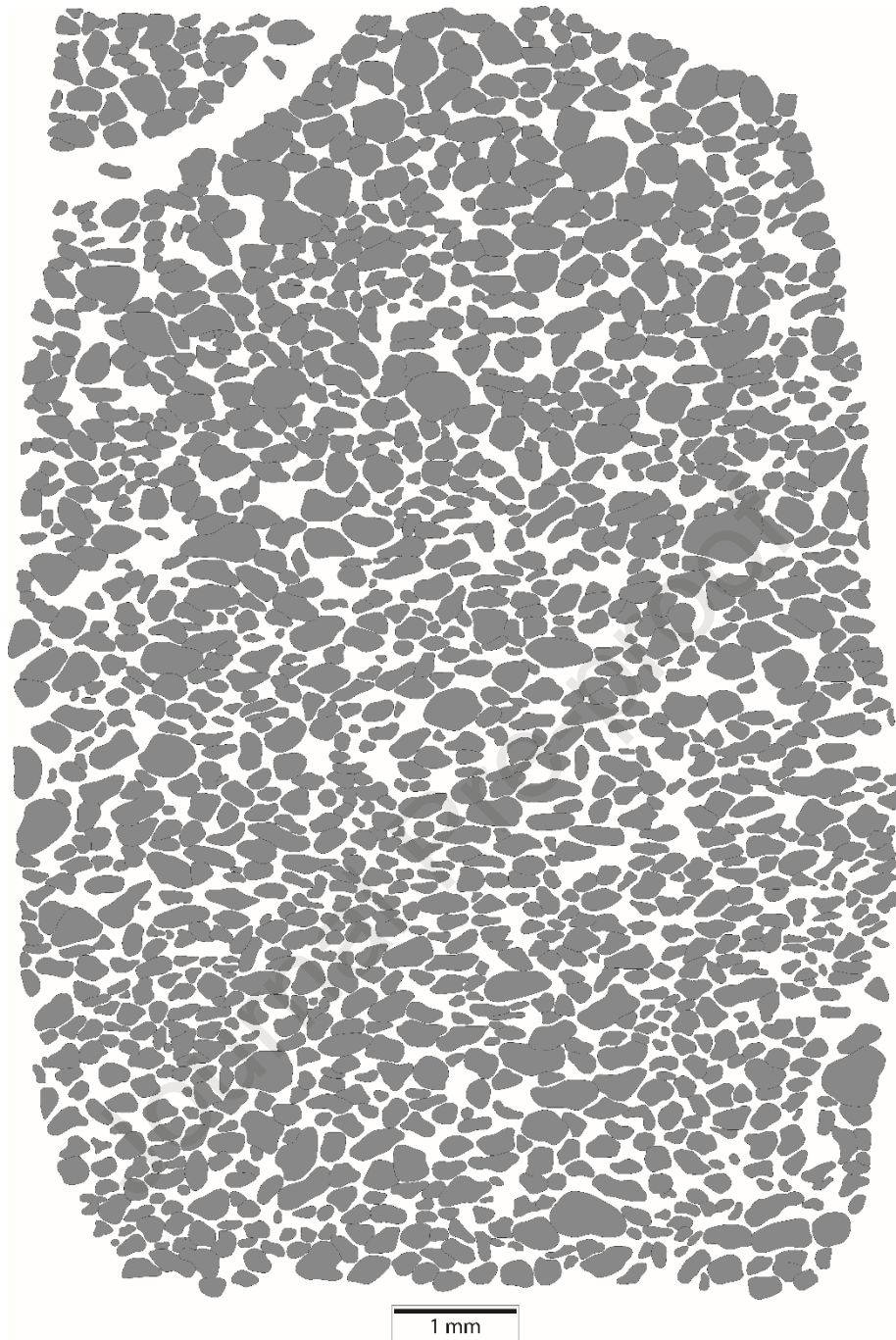


Figure 9. Example of the manual segmentation made for the OR62 (2000 MPa) thin section from optical cathodoluminescence images. Interiors of grains are isolated from the surrounding cement based on their luminescence colour contrasts. The shortening direction is vertical.

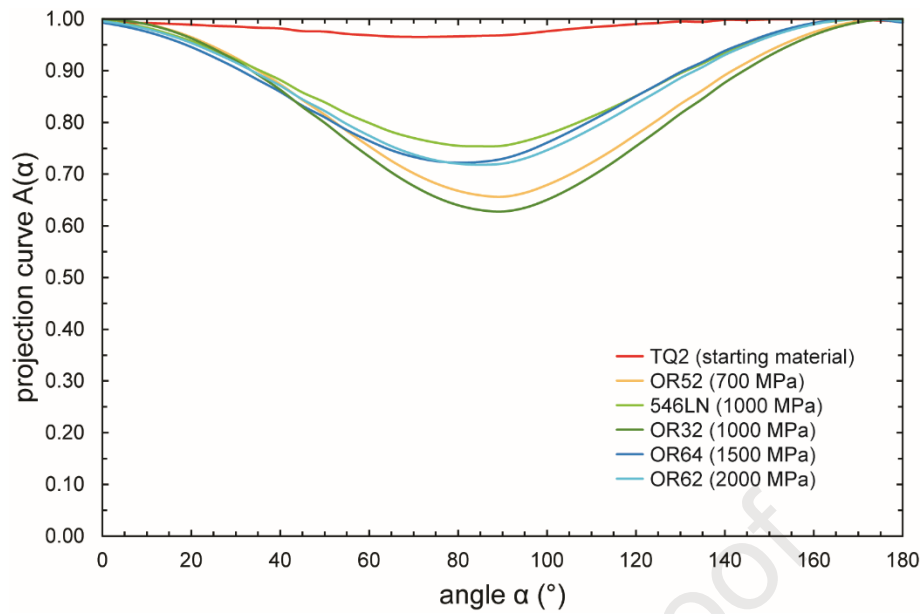


Figure 10. SURFOR projections curves showing that the starting material TQ2 has a slight strain of 3.5% whereas deformed samples at various confining pressures have an orientation comprise between 80 and 90° for a strain comprise between 24.6% (546LN) and 34.4% (OR52). The global shortening direction for deformed samples is theoretically 90°.

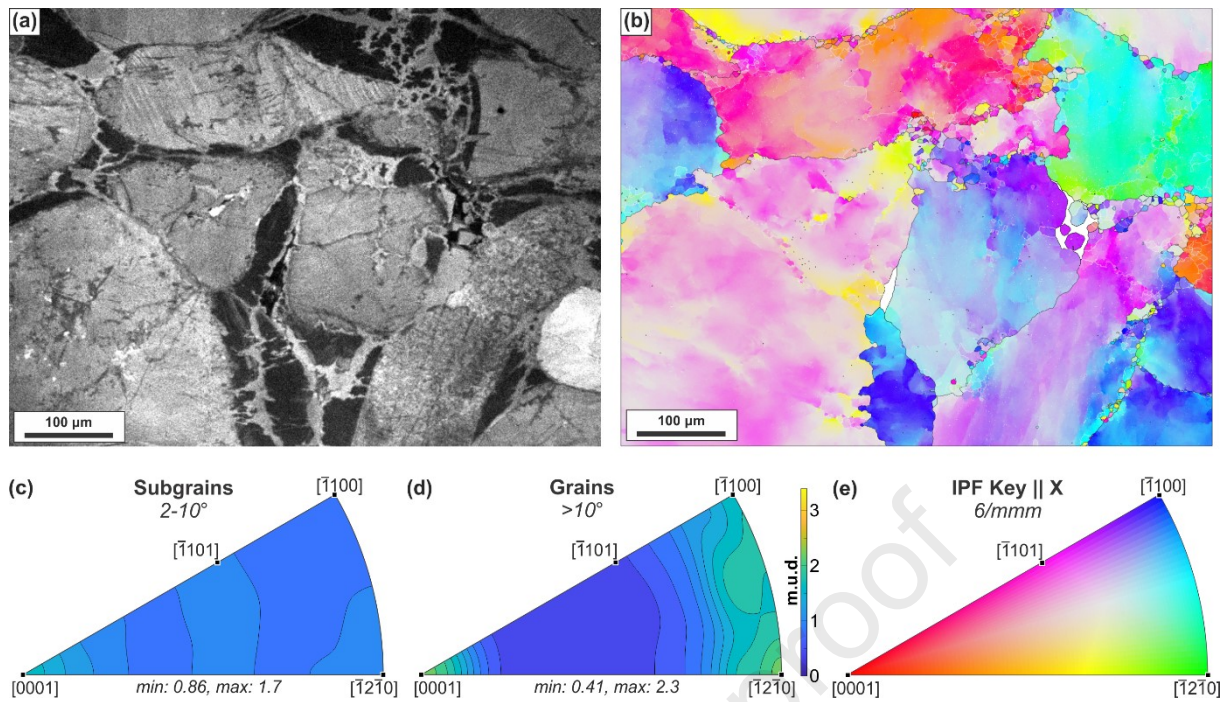


Figure 11. Cathodoluminescence (CL) image, EBSD orientation map and inverse pole figures (IPF) for sample 546LN. (a) CL image with blue (380-515 nm) optical filter to highlight recrystallized areas; (b) EBSD map of quartz orientations coloured parallel to the X direction, sample is plotted with hexagonal symmetry (6/mmm) to account for the effect of Dauphiné twins. Grain boundaries are identified by black bounding lines and subgrains are identified by white boundaries. (c) IPF's for subgrain (defined by a misorientation between 2 and 10°) boundaries and (d) grain (defined by a misorientation greater than 10°) boundaries. All IPF's are plotted in hexagonal 6/mmm symmetry with the same scale for multiples of uniform (m.u.d.) for each plot. (e) Colour key for IPF || X map.

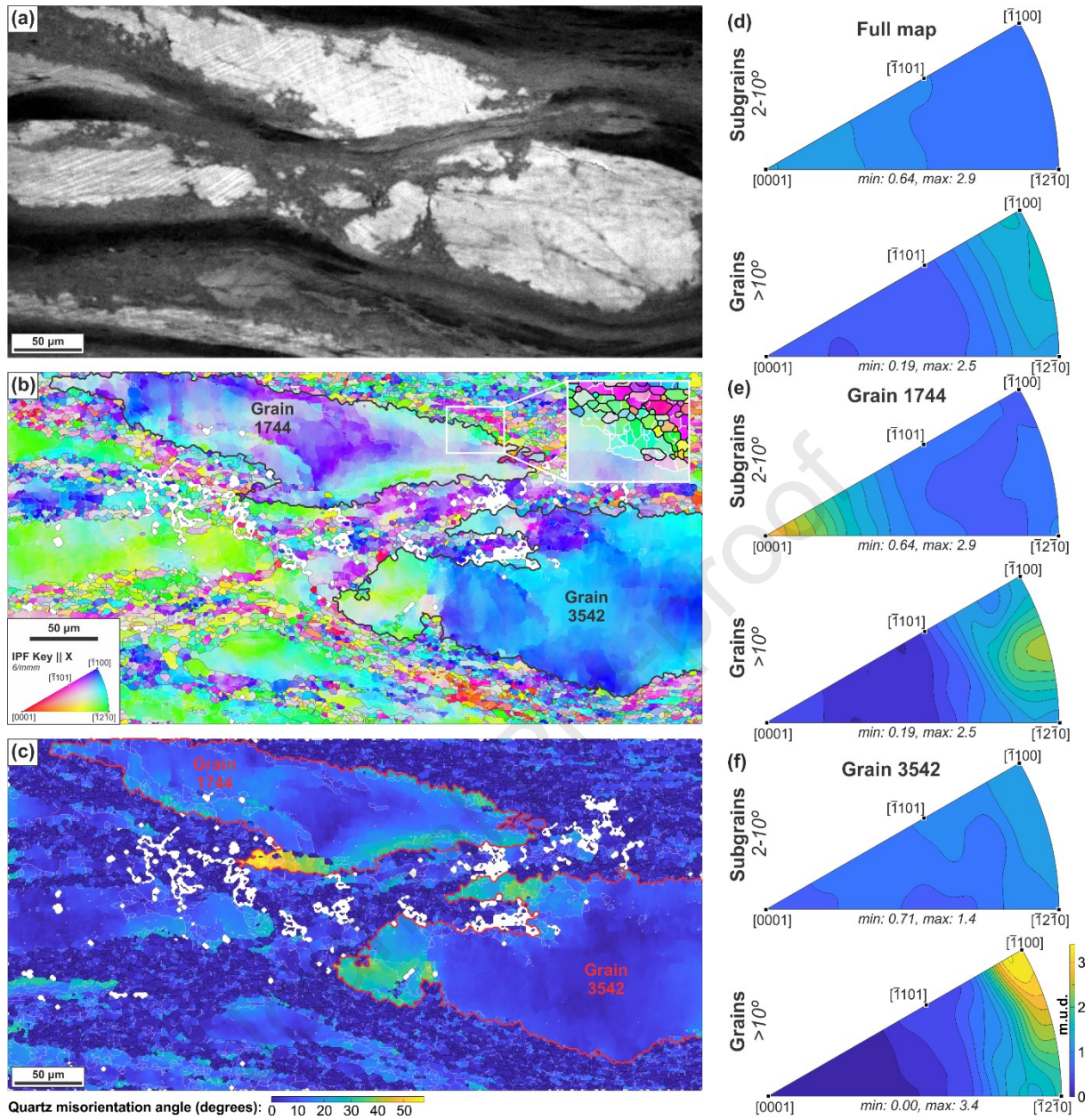


Figure 12. Cathodoluminescence (CL) image, EBSD orientation map, misorientation map and inverse pole figures (IPF) for high strain sample OR56. (a) CL image with blue (380-515 nm) filter to highlight recrystallized areas. (b) EBSD map of quartz orientations coloured parallel to the X direction, sample is plotted with hexagonal symmetry (6/mmm) to account for the effects of Dauphiné twins. Grain boundaries are identified by black bounding lines and subgrains are identified by white boundaries (see detailed insert at the top right hand corner). (c) Misorientation map where blue shows low misorientation and yellow shows high misorientation relative to the mean grain orientation. Grains 1744 and 3542 are highlighted on the IPF (bold black) and misorientation (red) maps. (d-f) IPF's for subgrain (defined by a misorientation between 2 and 10°) and grain (defined by a misorientation greater than 10°) boundaries with the d) full map, (e) grain 1744 and (f) grain 3542. All IPF's are plotted in hexagonal 6/mmm symmetry with the same scale for multiples of uniform distribution (m.u.d.) for each plot.

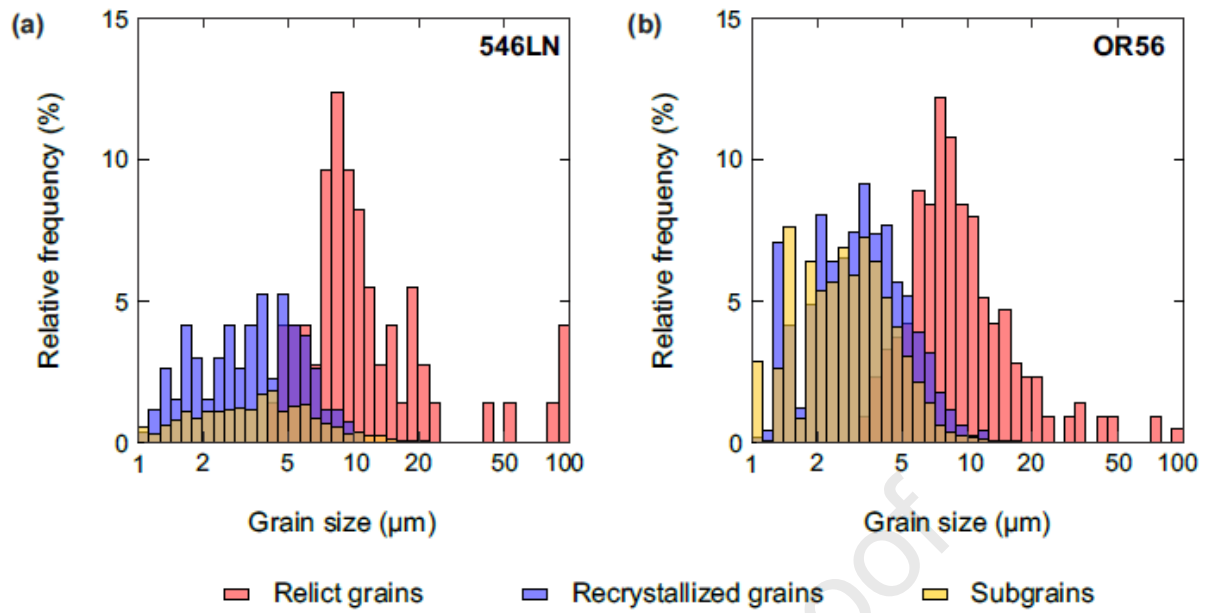


Figure 13. Log_{10} grain size distributions for samples (a) 546LN and (b) OR56. Grain size distributions are separated into relict, recrystallized and subgrain populations.

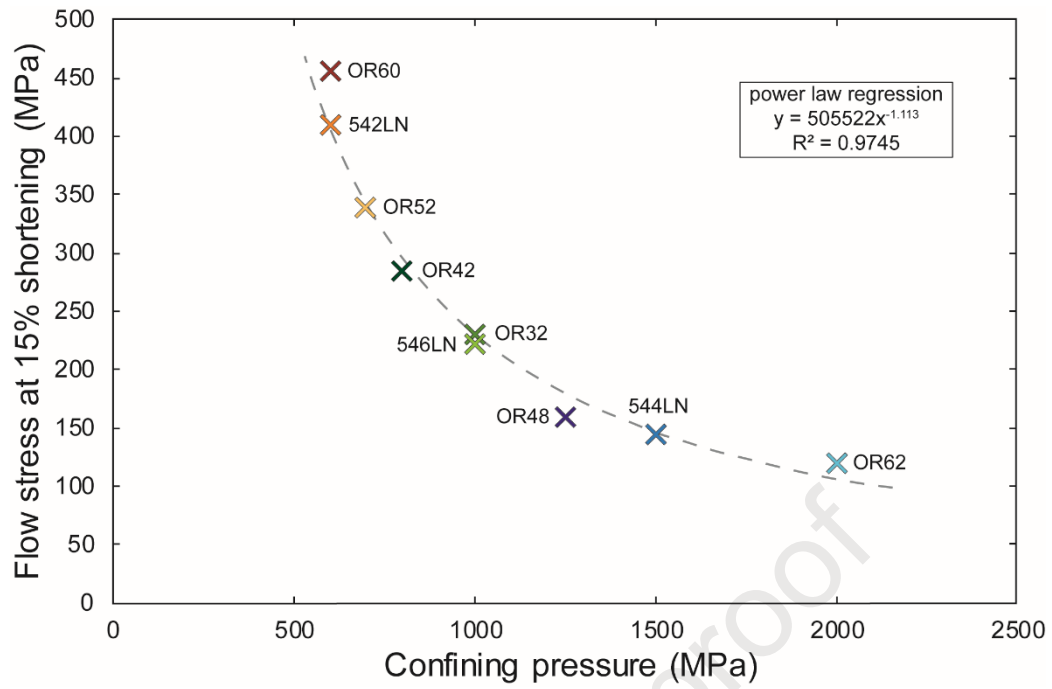


Figure 14. A power-law relationship fitted to the flow stresses (at 15% strain) at different confining pressures.

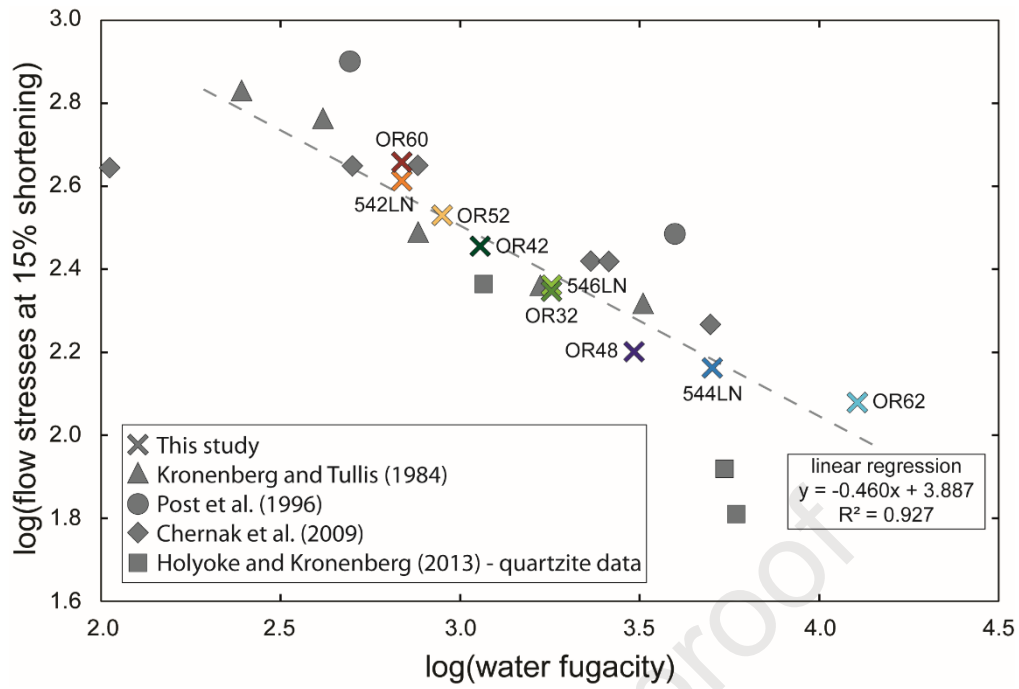


Figure 15. Relationship between water fugacity and flow stresses. The slope indicates a m/n coefficient of 0.46 for the values obtained in this study for Tana quartzite. Results from published studies are included for comparison.

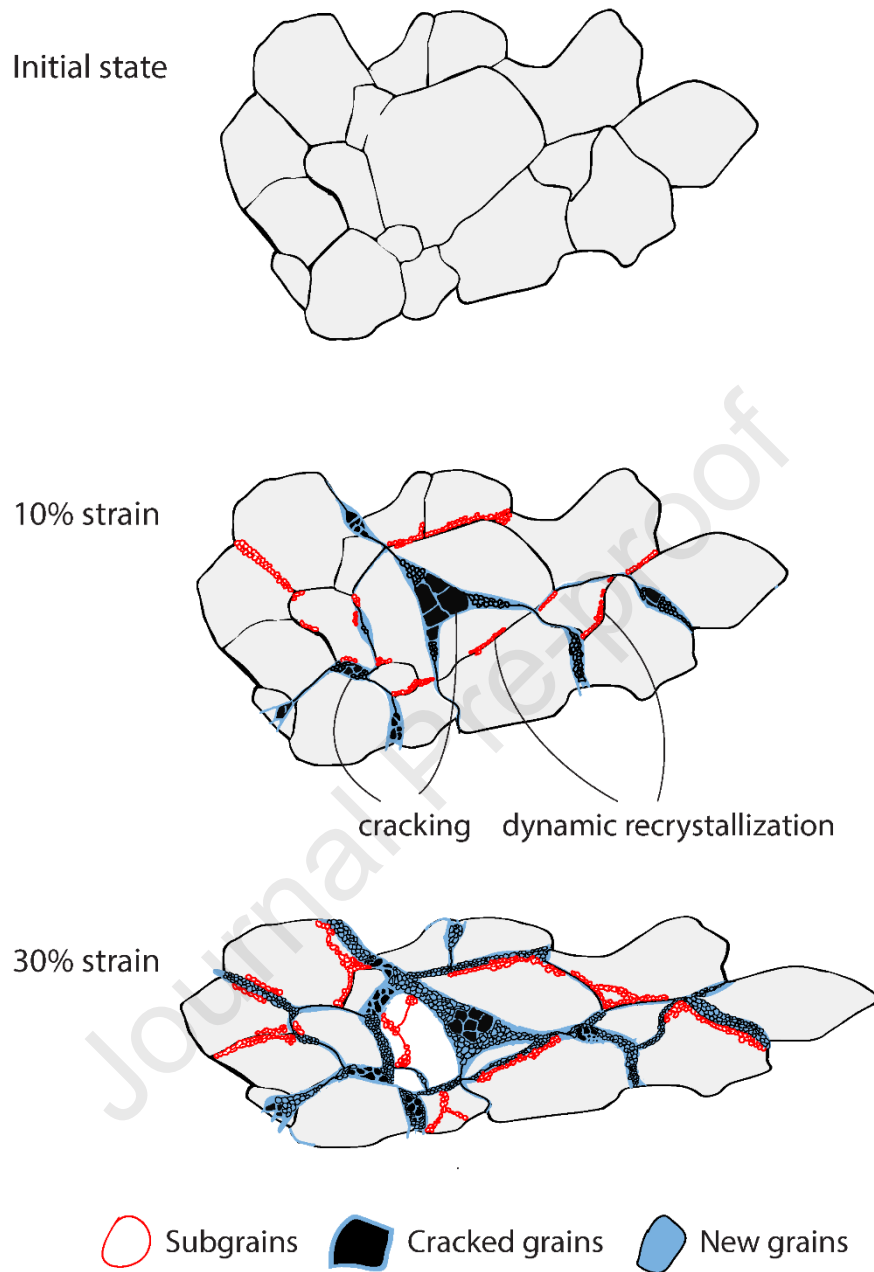


Figure 16. Sketch of the grain assemblage evolution during deformation.

Highlights

Inverse pressure dependence of flow stress in experimentally deformed quartzite

Bulk strain is accommodated by grain crystal plasticity

Recrystallization results from combined subgrain rotation and mode I cracking

Recrystallization processes are discriminated using cathodoluminescence of quartz

Pressure enhances grain boundary migration and reduces flow stress

Journal Pre-proof

Declaration of interests

The authors declare that they have no known competing financial interests or personal relationships that could have appeared to influence the work reported in this paper.

The authors declare the following financial interests/personal relationships which may be considered as potential competing interests:

Journal Pre-proof